

Electrostatic and Electromagnetic Turbulence
Associated with the Earth's Bow Shock

by

Paul Rodriguez

A thesis submitted in partial fulfillment of the
requirements for the degree of Doctor of Philosophy
in the Department of Physics and Astronomy
in the Graduate College of
The University of Iowa

July, 1974

Thesis supervisor: Professor Donald A. Gurnett

Graduate College
The University of Iowa
Iowa City, Iowa

CERTIFICATE OF APPROVAL

PH.D. THESIS

This is to certify that the Ph.D. thesis of

Paul Rodriguez

has been approved by the Examining Committee
for the thesis requirement for the Doctor of
Philosophy degree in the Department of Physics
and Astronomy at the July, 1974, graduation.

Thesis committee: Donald A. Hewitt
Thesis supervisor
Noah Hershenovitz
Member
L. A. Frank
Member
J. O. Norbury
Member
Karl Elser
Member

ACKNOWLEDGMENTS

In grateful appreciation to the many people who have made my research efforts possible, I wish to acknowledge their part in this work. I extend my thanks to Dr. D. Gurnett, who has been my advisor throughout my graduate career at the University of Iowa, and who has served me as the model of a researcher and teacher par excellence. Without his support and advice any merit to my efforts would have been greatly diminished. I also thank the students and workers of the VLF group, in particular Messrs. W. Kurth, G. Voots, and R. West, who took care of so much of the dreary work of data analysis, and Mrs. S. Van Engelenhoven, who typed the manuscript. Thanks are also extended to my fellow laborers Messrs. R. Shaw and R. Anderson, whose work on the IMP-6 project has made mine easier.

Among the other IMP-6 researchers, I thank Drs. N. Ness and D. Fairfield for providing the magnetometer data, and Drs. S. Bame and W. Feldman, whose particle data was used to obtain the shock parameters.

I also wish to express special thanks to Dr. J. Van Allen, who first made it possible for me to come to the University of Iowa.

This work was supported in part by the National Aeronautics and Space Administration under Contracts NAS5-1107 and NAS5-11431 and Grant NGL-16-001-043 and by the Office of Naval Research under Grant N00014-68-A-0196-0009.

ABSTRACT

The electric and magnetic field spectral densities of plasma waves in the earth's bow shock have been measured in the frequency range 20 Hz to 200 kHz using two 16-channel spectrum analyzers on the IMP-6 spacecraft. The electric field spectrum in the bow shock consists of two distinct components: one component has a broad peak typically centered between 200 to 800 Hz with an average (5.12 second time constant) spectral density at the peak of about 10^{-9} volt² m⁻² Hz⁻¹ and the other component increases monotonically with decreasing frequency approximately as $f^{-(2.0 \pm 0.5)}$ and has an average spectral density of about 3.0×10^{-9} volts² m⁻² Hz⁻¹ at 36.0 Hz. The magnetic field spectrum in the shock has only one component which increases monotonically with decreasing frequency approximately as $f^{-(4.0 \pm 0.5)}$ and has an upper cutoff frequency near the local electron gyrofrequency. This magnetic field spectrum appears to be associated with the monotonic component of the electric field spectrum. The electric to magnetic energy density ratio of this noise, $(E^2/8\pi)/(B^2/8\pi)$, is about 10^{-3} to 10^{-4} , which is consistent with the energy density ratio expected for electromagnetic whistler mode waves in the bow shock. The broad peak in the electric field spectrum at about 200 to 800 Hz has a large electric to magnetic energy density ratio, $\sim 10^2$ to 10^3 , indicating that this component consists of almost purely electrostatic waves.

Electrostatic noise with a spectrum similar to the turbulence in the shock, but with lower intensities, is observed throughout the magnetosheath region, downstream of the shock. This magnetosheath electric field turbulence often includes many bursts with a distinct parabolic frequency-time variation on a time scale of a few seconds. Spin modulation measurements of the electric field direction show that the electric field vectors in both the shock transition region and in the magnetosheath region are preferentially oriented parallel to the static magnetic field direction. The electric field of upstream electron plasma oscillations also is oriented parallel to the static magnetic field.

The intensity of the electrostatic component of turbulence in the bow shock increases as the upstream electron to ion temperature ratio T_e/T_i increases, and decreases as the upstream sound velocity C_s increases; both of these variations for the electrostatic component are consistent with ion sound wave turbulence. The electric field intensity of the electromagnetic component of shock turbulence has a weaker, but similar, variation with T_e/T_i and C_s , indicating that whistler waves couple to ion sound waves in the transition region. Both perpendicular and oblique shocks have the same characteristic spectra of electrostatic and electromagnetic turbulence.

TABLE OF CONTENTS

	Page
LIST OF TABLES	vii
LIST OF FIGURES	viii
I. INTRODUCTION	1
II. EXPERIMENT DESCRIPTION	4
A. Electric Antennas	4
B. Magnetic Antennas	5
C. Spectrum Analyzers	5
D. Wideband Receivers	6
III. PLASMA SHOCK WAVE THEORY	8
A. The MHD Approximation	8
B. The Two-Fluid Plasma	18
C. Plasma Wave Turbulence	24
IV. PLASMA WAVE SPECTRA IN THE BOW SHOCK	34
A. General Characteristics	34
B. Electric and Magnetic Fields Spectra in the Bow Shock	38
C. Electric to Magnetic Energy Density Ratio	43
D. High Resolution Spectra	46

TABLE OF CONTENTS (cont'd.)

	Page
V. ELECTRIC FIELD POLARIZATION	48
A. Upstream Electron Plasma Oscillations	49
B. Electrostatic Waves in the Bow Shock	51
C. Electrostatic Turbulence in the Magnetosheath . .	54
VI. INTENSITY VARIABILITY OF SHOCK TURBULENCE	56
A. Correlation with Upstream State	56
B. Electric Field Strength Dependence	57
C. Magnetic Field Turbulence	59
VII. SUMMARY OF RESULTS AND CONCLUSIONS	60
LIST OF REFERENCES	67
APPENDIX A: TABLES	71
APPENDIX B: FIGURES	73

LIST OF TABLES

	Page
TABLE 1. Linear Correlation Coefficient, R	72

LIST OF FIGURES

	Page
Figure 1 IMP-6 Spacecraft schematic.	74
Figure 2 Block diagram of IMP-6 plasma wave experiment. . .	76
Figure 3 MHD wave modes. Polar plots showing the dependence of the propagation speeds of the three linear wave modes on the angle between the wave normal and the magnetic field for several values of the ratio of sound speed C_s to Alfven speed C_A . The speeds are normalized with respect to $(C_s^2 + C_A^2)^{1/2}$. [After Kantrowitz and Petschek, 1966.]	78
Figure 4 The three solutions to the two-fluid dispersion relation for a warm plasma, propagation direction with respect to the magnetic field $\theta = 45^\circ$, and $C_s^2/C_A^2 = 0.2$. The wave frequency ω is normalized to the ion gyrofrequency Ω_+ and the wave number k to C_s/Ω_+ . The dashed line labelled C_e estimates the electron thermal velocity for a hydrogen plasma with equal ion and electron temperatures. The lower left hand corner is the domain of validity	

LIST OF FIGURES (cont'd.)

Page

for the MHD approximation. Below the ion gyrofrequency the three MHD waves propagate; between the electron and ion gyrofrequencies, the whistler and ion sound waves propagate; above the electron gyrofrequency the ion sound wave propagates. Coupling points occur near the electron and proton gyrofrequencies. The approximate expressions shown for the phase velocities are strictly valid only when $C_s^2/C_A^2 \ll 1$. [After Formisano and Kennel, 1969.] 80

Figure 5 The properties of warm plasma propagation in ω/Ω_+ , C_s^2/C_A^2 parameter space. In each region is a polar plot whose radius is the plane wave phase velocity and whose angle is the angle of propagation relative to the magnetic field. The direction of the magnetic field is denoted by an arrow. The dotted reference circles have a radius C_s . The interaction diagonal indicates where the cold plasma parallel whistler phase velocity equals the sound speed. Parallel sound waves are slower than whistlers to the

LIST OF FIGURES (cont'd.)

	Page
left and faster to the right of this line. [After Formisano and Kennel, 1969.]	82
Figure 6 A schematic diagram of the perpendicular shock model with $\vec{B}(x) = B(x)\hat{z}$ and $\vec{E} = E\hat{x}$. The magnetic field gradient $\nabla B = \partial B/\partial x (-\hat{x})$ is related to the net electron drift current by $(4\pi/c)\vec{J} = \nabla \times \vec{B}$. The electric field is determined by charge separation. The guiding center trajectories in the x-y plane of ions (i) and electrons (e) indicate that only electrons undergo appreciable drift motion over the shock thickness scale length L_s	84
Figure 7 A typical bow shock crossing as detected by the IMP-6 plasma wave experiment. Average measurements (5.12 second time constant) are plotted as vertical lines; peak measurements (0.1 second time constant) are plotted as dots. The shock transition occurs at about 1048 UT. The electric field measurements (left) show upstream plasma oscillations at 31.1 kHz after 1048 UT. Shock parameters, $M_A = 7.7$, $\beta = 0.89$, $T_e/T_i = 3.3$, $\psi(\vec{B}, \hat{n}) = 73^\circ$	86

LIST OF FIGURES (cont'd.)

	Page
Figure 8 A double crossing of the earth's bow shock as detected by the IMP-6 plasma wave experiment. The bow shock was very nearly a perpendicular shock during these crossings. Shock parameters, $M_A = 6.0$, $\beta = 0.54$, $T_e/T_i = 3.3$, $\psi(\vec{B}, \hat{n}) = 92^\circ$. . .	88
Figure 9 The electric field spectra, based on average measurements, for the crossing at 1252 UT in Figure 8. The time indicated is for the first spectrum with the averaging time, 5.12 seconds between succeeding spectra thereafter. Snapshot 7 is the shock electric field spectrum. . . .	90
Figure 10 The magnetic field spectra, based on average measurements, for the crossing at 1252 UT in Figure 8 and corresponding to the electric field spectra in Figure 9. Snapshot 6 is the shock magnetic field spectrum.	92
Figure 11 The shock electric field spectrum $E^2(w)_{sh}$ selected on the basis of r. m. s. electric field amplitude. The peak spectrum obtained during the averaging time of the average	

LIST OF FIGURES (cont'd.)

	Page
measurements is also shown. The two distinct components in the shock electric field spectrum are shown by dashed lines.	94
Figure 12 The shock magnetic field spectrum $B^2(\omega)_{sh}$ for the shock crossing of 1252 UT. The characteristic frequency dependence f^{-4} is present in both peak and average spectra. The electron gyrofrequency $f_{ge} \sim 350$ Hz.	96
Figure 13 A representative distribution of electric field shock spectra, average and peak measurements. The average spectra show that the broad peak in the electric field spectra becomes more distinct as the overall intensity of the spectra increases up to some intermediate range, and then becomes less distinct as the very low frequency electric field spectral density saturates. The peak spectra are generally similar to the average spectra in shape, but range up to an order of magnitude more intense.	98

LIST OF FIGURES (cont'd.)

	Page
Figure 14 Representative distribution of magnetic field shock spectra, average and peak measurements, corresponding to the electric field spectra of Figure 13. Some of the peak spectra indicate the presence of distinct wave modes.	100
Figure 15 The ratio of electric energy density to magnetic energy density for the shock crossing of 1252 UT, Figure 8. The low frequency portion of snapshots 5, 6, and 7 is consistent with whistler waves. At higher frequencies electrostatic noise is the dominant wave mode. The region of electrostatic noise is observed to broaden toward lower frequencies further into the transition region.	102
Figure 16 A representative distribution of energy density ratios for 10 shock crossings, selected at random from the shock electric and magnetic field spectra.	104

LIST OF FIGURES (cont'd.)

	Page
Figure 17 Wideband spectra for the shock crossings of Figure 8, for frequencies 0 - 500 Hz. The turbulence of the shock transition appears more homogeneous than downstream turbulence for both electric and magnetic fields. Discrete noise structure characterizes the downstream regions.	106
Figure 18 Expanded time scale wideband spectra for the second shock crossing of Figures 8 and 17. The shock turbulence retains a homogeneous appearance, while the downstream noise shows a few 'parabola shaped' bursts in the electric field.	108
Figure 19 Upstream electron plasma oscillations and 'pre-cursor' encountered a few minutes before the shock crossing at about 1548:30 UT. The rapid sample measurements A and B give the spin modulated electric field amplitudes shown in the two polar plots with the electric field vector predominantly aligned parallel to the static	

LIST OF FIGURES (cont'd.)

	Page
magnetic field. Shock parameters, $M_A = 4.8$, $\beta = 0.34$, $T_e/T_i = 3.3$, $\psi(\vec{B}, \hat{n}) = 111^\circ$	110
Figure 20 Rapid-sample measurement of electric field at 3.11 kHz for the bow shock transition and downstream regions. The electric field fluctua- tions are correlated with magnetic field gradients in both the transition and downstream regions. The polar plot in the upper right corner shows the spin modulation of electric field amplitude for the transition region, interval a to b. The downstream electric field fluctuations, indicated by the envelope of exponential decay, do not show spin modulation effects (middle and lower right polar plots). Shock parameters, $M_A = 4.8$, $\beta = 0.28$, $T_e/T_i = 6.7$, $\psi(\vec{B}, \hat{n}) = 87^\circ$	112
Figure 21 A series of rapid-sample measurements of the magnetosheath electric field turbulence which shows that the electric field vector of this noise is aligned parallel to the static mag- netic field. Shock parameters, $M_A = 1.8$, $\beta = 0.03$, $T_e/T_i = 4.0$, $\psi(\vec{B}, \hat{n}) = 95^\circ$	114

LIST OF FIGURES (cont'd.)

Page

Figure 22 The plot of $E_{rms,2}$ against T_e/T_i which shows a strong positive correlation. The dashed diagonal line is the line of regression for a least squares fit to the equation $\log y = ax + b$, where $y = E_{rms,2}$ and $x = T_e/T_i$. The degree of dispersion of the slope of the regression line, which is the important measure of association, is indicated by the small error bars at $\pm 2.576 \sigma(\bar{y})$. Correlations with parameters not included in this fit contribute to the large error bars at $\pm \sigma(y)$. The solid diagonal line indicates an apparent lower threshold for electrostatic turbulence. 116

Figure 23 The plot of $E_{rms,2}$ against C_s (proportional to $(T_e + T_i)^{1/2}$) showing a strong negative correlation for a least squares fit to $\log y = ax + b$ where $y = E_{rms,2}$ and $x = C_s$. The error bars have the same meaning as in Figure 22. 118

LIST OF FIGURES (cont'd.)

	Page
Figure 24 The plot of $E_{rms,1}$ against C_s (proportional to $(T_e + T_i)^{1/2}$) showing a negative correlation almost as strong as for $E_{rms,2}$ and C_s . The error bars have the same meaning as in Figure 22.	120
Figure 25 The plot of B_{rms} against $\psi(\vec{B}, \vec{V}_{SW})$, the angle between the upstream vectors of magnetic field and solar wind velocity. $\psi(\vec{B}, \vec{V}_{SW})$ is the only angle with which shock turbulence had a significant correlation. The error bars have the same meaning as in Figure 22.	122

I. INTRODUCTION

A basic problem of shocks in collisionless plasmas is to identify and understand the dissipation mechanism that occurs in the transition region connecting the upstream and downstream states. In the absence of binary collisions dissipation must occur through collective Coulomb interactions of the charged particles. This results in the self-consistent generation of a turbulent spectrum of electrostatic waves that stochastically accelerates the charged particles. Experimentally, this is often described in terms of an 'anomalous' or effective resistivity for Ohm's law, $\vec{E} = \eta^* \vec{J}$, through which turbulent electric fields heat the plasma. The earth's bow shock provides a very convenient steady-state laboratory for the study of high Mach number collisionless shocks. Electron and proton velocity distributions measured in the solar wind and magnetosheath near the bow shock indicate that strong thermalization occurs in relatively thin regions within the shock structure [Montgomery et al., 1970; Formisano and Hedgecock, 1973a, b]. Magnetometer measurements of the magnetic field in the bow shock up to 10 Hz show a broad turbulent spectrum 2-3 orders of magnitude above the interplanetary spectrum [Olson et al., 1969; Holzer et al., 1966, 1972]. Electric field spectra in the range 560 Hz to 70 kHz [Fredricks et al., 1968,

1970a, b] show electrostatic turbulence in the shock strongly correlated with magnetic field gradients, indicating the presence of some form of current-driven instability [Wu and Fredricks, 1972].

In this report we present some simultaneous measurements of electric and magnetic field spectral densities in the bow shock as obtained with the University of Iowa plasma waves experiment on the IMP-6 spacecraft. The frequency range of the plasma wave detector, 20 Hz to 200 kHz, covers most of the characteristic plasma frequencies for electrons and protons in average solar wind conditions. Electric fields are measured with long dipole antennas (~ 100 meters tip-to-tip) with high sensitivity, on the order of 1 microvolt/meter. Magnetic fields are measured with single-turn loop antennas.

The electric field measurements of Fredricks et al. [1968] were obtained with short dipole antennas (effective length 0.5 meters) on the OGO-5 spacecraft, which are less sensitive than the long IMP-6 antennas (ratio of effective lengths ~ 100). To provide a basis for comparison with the OGO-5 measurements IMP-6 also has a short dipole antenna (effective length 0.38 meters).

The IMP-6 spacecraft was launched on March 13, 1971, with initial orbit parameters as follows: period, 4.18 days; perigee, 6614 km; apogee, 212,269 km ($\sim 34 R_e$); inclination, 28.7° . The satellite is spin stabilized with its spin vector perpendicular to the ecliptic plane and pointing toward the south celestial pole, with a nominal spin period of 11.1 seconds.

The measurements of the present study were obtained during the first thirty orbits, covering the noon to dawn quadrant of local time. During this time, from March 17, 1971, to July 15, 1971, the solar wind conditions were usually relatively quiet, with intermittent noisy periods as indicated by daily average values of K_p . The overall average K_p was about 2.0. In thirty orbits the spacecraft would have to cross the shock at least 60 times, but multiple crossings (due to the bow shock structure moving in oscillatory motion past the spacecraft) have increased this number to over 150.

II. EXPERIMENT DESCRIPTION

A. Electric Antennas

The spacecraft has three mutually perpendicular long dipole antennas identified in the spacecraft frame as $\underline{+X}$, $\underline{+Y}$, and $\underline{+Z}$. The spacecraft spin vector is in the $\underline{+Z}$ direction and the X-Y plane is parallel to the ecliptic plane. The antennas are formed from pre-stressed conducting ribbons, that assume a tubular shape as they are extended outwards from the spacecraft. An insulating material covers all but the outer 16.8 m of the antennas. Extensions of the antennas were made in seven steps over the time interval of the first nine orbits. The final tip-to-tip lengths are as follows: $E_X = 54.0$ m, $E_Y = 93.2$ m, $E_Z = 7.7$ m. The effective lengths for the long antennas are taken as one-half the tip-to-tip lengths. The short dipole antenna (SE) is attached to the magnetometer boom and oriented along the Z direction. Two spherical wire cages at the ends of insulating rods form the elements of the short dipole antenna, giving it an effective length of 0.38 m. This antenna was designed to serve as a back-up to the long antennas and to provide the measurements at a different effective length. Figure 1 shows a schematic drawing of the spacecraft.

B. Magnetic Antennas

A system of three orthogonal loops at the end of a boom form the magnetic antennas (M_X , M_Y , M_Z). They are oriented to conform to the coordinate system defined by the long electric antennas. Each loop is made of a single turn of aluminum tubing and has an area of 0.81 m^2 .

C. Spectrum Analyzers

Two 16-channel spectrum analyzers (A and B) are used to provide spectrum measurements. Each spectrum analyzer covers the frequency range from 20 Hz to 200 kHz with four filters per decade of frequency. The filter bandwidths range from about 20% of the center frequency at low frequencies to about 10% at high frequencies. Each filter is connected to a logarithmic receiver with 100 db dynamic range and 10 μ volt sensitivity. The receiver output is proportional to the logarithm of the input voltage. Using the long electric antenna, electric fields as low as 0.2 microvolts/meter can be detected. The magnetic field sensitivities depend on the wave frequency and range from 2.0 milligammas at 36 Hz to about 10.0 microgammas at 16.5 kHz. A block diagram of the plasma wave experiment is shown in Figure 2.

In the usual mode of operation analyzer A is connected to the E_Y antenna and analyzer B is connected to the M_X antenna. However, on command each analyzer can be switched to any of the seven available antennas. In the high-rate data sampling mode, the 32 analyzer channels are sampled in rapid sequence once every 5.12

seconds for average and peak outputs. The peak measurement gives the maximum receiver output over the 5.12 second interval between samples. The time constants are 5.12 seconds for the average measurement and 0.10 second for the peak measurement. A complete set of average and peak spectrum measurements is obtained for all channels once every 5.12 seconds and is called a snapshot. A snapshot is the basic data unit for the spectral density calculations presented in this paper. In addition to the spectrum measurements, there is a rapid-sample mode in which a given channel is sampled every 0.32 seconds. The rapid-sample measurements cycle through 8 spectrum analyzer channels in a fixed sequence, giving 128 consecutive samples from a given channel.

Shortly after launch, it was determined that intense low-frequency (below 1 kHz) electric field interference was being produced by the spacecraft solar array. The main component of this noise is strongly spin modulated and is due to voltage transients caused by the shadow of the magnetic antenna boom and loops moving across the solar cell panels. The near 2:1 relationship between the spacecraft spin period (11.1 sec) and the sampling interval (5.12 sec) means that noise contamination in the peak measurements occurs in alternate snapshots, and is easily identified.

D. Wideband Receivers

Two wideband receivers provide broadband coverage over the ranges 10 Hz to 1 kHz and 650 Hz to 30 kHz. These analog signals

are used to reconstruct analog frequency-time spectra for studying cutoffs, resonances, and other wave characteristics which require good frequency-time resolution.

III. PLASMA SHOCK WAVE THEORY

A. The MHD Approximation

A small amplitude pulse propagating through a fluid may be viewed as the propagation of a small gradient in some plasma property, for example the pressure. If the phase velocities of the wave components of the pulse are proportional to the pressure, then where the pressure is slightly greater the waves travel slightly faster. Thus the higher pressure portions of the pulse move ahead of the lower pressure portions, increasing the gradient of the pressure and the pulse is said to steepen. The steepening of the pulse produces more waves travelling faster, which causes further steepening. This process continues until dissipative mechanisms, proportional to the pressure gradient, become strong enough to stop the steepening and establish an equilibrium gradient. For large enough amplitudes the propagating pressure gradient can become a shock wave travelling with a velocity greater than that of a small amplitude wave in the undisturbed fluid.

The process by which a shock wave is formed depends upon the nonlinear properties of the wave, i.e., the phase velocities of the component waves are proportional to a quantity which is changed by the waves. If we consider only very small amplitude waves, then the nonlinear equations of motion that describe the fluid may be linearized and solved for the elementary modes of oscillation of the fluid.

These elementary modes may then be used as a basis for studying the nonlinear waves.

For shocks in a magnetized plasma the magnetohydrodynamic (MHD) waves for frequencies $\omega < \Omega_i$ ($\Omega_i = eB/m_i c$, the lowest ion gyrofrequency) form the elementary modes of the plasma. Considering the plasma as a perfectly conducting, nondissipative fluid, the ideal MHD equations are

$$\frac{\partial \rho}{\partial t} + \nabla \cdot (\rho \vec{v}) = 0 \quad (1)$$

$$\rho \frac{\partial \vec{v}}{\partial t} + \rho \vec{v} \cdot \nabla \vec{v} + \nabla p - \frac{1}{c} (\vec{j} \times \vec{B}) = 0 \quad (2)$$

$$\frac{\partial \vec{B}}{\partial t} - \nabla \times (\vec{v} \times \vec{B}) = 0 \quad (3)$$

$$\frac{\partial}{\partial t} \left(\frac{p}{\rho \gamma} \right) + \vec{v} \cdot \nabla \left(\frac{p}{\rho \gamma} \right) = 0 \quad (4)$$

$$\nabla \cdot \vec{B} = 0 \quad (5)$$

$$\nabla \times \vec{B} = \frac{4\pi}{c} \vec{j} \quad (6)$$

where ρ is the mass density, \vec{v} the fluid velocity, p the plasma pressure and γ is the ratio of specific heats c_p/c_v . \vec{j} and \vec{B} are the current density and magnetic field intensity. The first four equations describe the mass flux, momentum flux, magnetic induction, and entropy conservation of the plasma. The last two equations are Maxwell's equations.

We assume a coordinate system in which the wave is stationary (wave phase velocity equal and opposite to the fluid velocity) and in which \vec{B} and \vec{v} define the x-y plane, $\vec{B} = (\vec{B}_x, \vec{B}_y, 0)$, $\vec{v} = (\vec{v}_x, 0, 0)$ and the z-axis is the perpendicular to this plane. The MHD equations may be linearized by assuming small perturbations (subscript 1) on the average quantities (subscript 0):

$$\rho = \rho_0 + \rho_1$$

$$\vec{v} = \vec{v}_0 + \vec{v}_1$$

$$p = p_0 + p_1$$

$$\vec{B} = \vec{B}_0 + \vec{B}_1$$

Taking only the first order equations that result, we may solve for the wave velocity $v_0 = v$ to obtain the dispersion relations [Kantrowitz and Petschek, 1966].

$$v^2 = c_A^2 \cos^2 \theta \quad (7)$$

$$(v^2 - c_s^2)(v^2 - c_A^2) = c_s^2 c_A^2 \sin^2 \theta \quad (8)$$

where $c_A^2 = B^2/4\pi\rho$ is the Alfven velocity, $c_s^2 = \gamma p/\rho$ is the sound velocity and θ is the angle between \vec{B} and the wave normal

$\hat{n}(= \vec{v}/|\vec{v}|)$. The dispersion relations (7) and (8) describe the three elementary modes of the MHD fluid and are named the fast, intermediate and slow waves, according to the magnitude of the velocity. The intermediate mode is given by (7). The fast and slow modes are given by (8), from which it may be shown that they satisfy the inequalities

$$v_f^2 \geq C_A^2, \quad v_f^2 \geq C_s^2$$

and

$$v_s^2 \leq C_A^2 \cos^2 \theta, \quad v_s^2 \leq C_s^2$$

where f and s indicate the fast and slow modes. The dispersion relations are plotted in Figure 3 for several ratios C_s^2/C_A^2 .

By considering the effect of a small amplitude intermediate wave on the plasma flow properties, it has been shown [Jeffery, 1966, Kantrowitz and Petschek, 1966] that this mode merely rotates the magnetic field component in the plane of the wave front and perpendicular to the direction of propagation, while leaving the density, pressure and normal component of velocity unchanged. Thus, large amplitude intermediate waves which do not steepen into shock waves are possible in a plasma. For small amplitude fast and slow waves it is found that the magnetic field remains in the plane defined by the wave normal and the magnetic field ahead of the wave (magnetic

coplanarity). In addition, the density, pressure and normal component of velocity change across both fast and slow modes, but in opposite directions. The changes in flow properties may be summarized as:

- a) The velocity changes across the three waves are mutually perpendicular.
- b) For the fast and slow modes, magnetic and velocity coplanarity holds, i.e., changes in the magnetic field and velocity remain in the planes defined by their upstream vectors and the wave normal vector. For the intermediate wave, the changes in the magnetic field and velocity vectors are perpendicular to these planes.
- c) For the fast wave, the density and magnetic pressure changes have the same sign, i.e., a compressive wave increases the magnetic pressure; for the slow wave, the changes have opposite sign; the intermediate wave produces no changes in magnetic pressure or density.

The flow properties of fast and slow waves indicate that for large amplitude waves, they tend to steepen into shock waves. Thus for $C_s^2 = \gamma p / \rho$ and $v_f \sim C_s$, $dv_f / v_f \sim dC_s / C_s = 1/2\sqrt{\gamma} (\gamma - 1) dp / p$, and for $dp > 0$ the wave velocity increases. On thermodynamics grounds, it may be shown [Jeffrey, 1966] that the entropy must increase across a shock and thus equation (4) does not hold for shocks. This restricts the flow properties of fast and slow shocks so that across a fast shock the density and magnetic pressure increase while across a slow shock the density increases and the magnetic pressure decreases.

From Figure 3 we can see that a perpendicular shock ($\hat{n} \perp \vec{B}$) must be a fast shock.

Given that a shock wave has formed in a plasma, we may obtain relations between the state variables on either side of the shock wave, independently of the dissipation processes which occur in the transition region where large gradients in the plasma variables exist. This is done by rewriting equations (1) - (3) and (5) in the form of conservation equations, $\partial U / \partial t + \nabla \cdot \vec{F} = A$ or $\partial U / \partial t + \nabla \cdot (\vec{F} - \vec{G}) = 0$ if $A = \nabla \cdot \vec{G}$, and integrating them from a position ahead of the shock (upstream) to a position behind the shock (downstream), at which points it may be assumed that steady state conditions ($\partial U / \partial t = 0$) prevail. These relations are called the jump conditions; the steady state assumption is equivalent to evaluating the jump conditions in the shock frame of reference.

In the form of conservation equations (1) - (3) and (5) become [Jeffrey, 1966]

$$\frac{\partial}{\partial t} \rho + \nabla \cdot (\rho \vec{v}) = 0$$

$$\frac{\partial}{\partial t} (\rho \vec{v}) + \nabla \cdot (\rho \vec{v} \vec{v}) + \nabla p^* - \frac{1}{4\pi} \nabla \cdot (\vec{B} \vec{B}) = 0$$

$$\frac{\partial}{\partial t} \vec{B} + \nabla \cdot (\vec{v} \vec{B} - \vec{B} \vec{v}) = 0$$

$$\frac{\partial}{\partial t} W + \nabla \cdot (\vec{v} W) + \nabla \cdot [p^* \vec{v} - \frac{\vec{B}(\vec{v} \cdot \vec{B})}{4\pi}] = 0$$

$$\nabla \cdot \vec{B} = 0$$

where $p^* = p + B^2/8\pi$ and where entropy conservation equation (4) (no longer valid for shocks) is replaced by the equation for energy flux conservation with $W = 1/2\rho v^2 + \rho u + B^2/8\pi$ (where W is the total energy and u is the internal energy). In the frame of the shock the time derivatives drop out and assuming that the shock front is a plane defined by the local shock normal vector \hat{n} , we may integrate the divergence terms across the shock front to get the jump conditions (or Rankine-Hugoniot relations)

$$[\rho \vec{v} \cdot \hat{n}] = 0 \quad (9)$$

$$[\rho \vec{v}(\vec{v} \cdot \hat{n}) + p^* \hat{n} - \frac{\vec{B}}{4\pi}(\vec{B} \cdot \hat{n})] = 0 \quad (10)$$

$$[\vec{v}(\vec{B} \cdot \hat{n}) - \vec{B}(\vec{v} \cdot \hat{n})] = 0 \quad (11)$$

$$[(W + p^*) \vec{v} \cdot \hat{n} - \frac{(\vec{v} \cdot \vec{B})(\vec{B} \cdot \hat{n})}{4\pi}] = 0 \quad (12)$$

$$[\vec{B} \cdot \hat{n}] = 0 \quad (13)$$

where $[x] = x_1 - x_2$; 1 and 2 refer to upstream and downstream sides of the shock.

If the jump conditions are to be evaluated between the upstream state and the shock transition, source terms must be included on the right hand side of equations (11) and (12) which are proportional to finite resistivity and energy dissipation, respectively.

These source terms come from Ohm's law $\vec{E} + 1/c(\vec{v} \times \vec{B}) = \eta^* \vec{J}$, where η^* is the anomalous resistivity, and from the energy conservation equation $\partial W/\partial t + \nabla \cdot \vec{s} = -\vec{E} \cdot \vec{J}$, where \vec{s} is the energy flux and $-\vec{E} \cdot \vec{J}$ is the energy dissipation. For each frequency component ω , the electric field \vec{E}_ω arises self-consistently from the currents \vec{J}_ω , resulting in the turbulent spectrum $\langle \vec{E}_\omega \cdot \vec{E}_\omega \rangle$ for shock dissipation.

The jump conditions show that shocks can be characterized by four variables, \vec{v} , \vec{B} , ρ , and p . Shocks may be described in a concise way by using the upstream values of these variables to define the following shock parameters:

$$M_A = \frac{v_1}{(B_1^2/4\pi\rho_1)^{1/2}} = \frac{v_1}{c_{A1}}$$

$$M_s = \frac{v_1}{(\gamma p_1/\rho_1)^{1/2}} = \frac{v_1}{c_{s1}}$$

$$\beta = \frac{p_1}{(B_1^2/8\pi)} = \frac{2}{\gamma} \frac{c_{s1}^2}{c_{A1}^2}$$

where M_A and M_s are the Alfvén and sound Mach numbers and must be greater than one for shocks, and β is the ratio of thermal to magnetic pressure. For $\gamma = 1$ the fluid acts isothermally, for $\gamma = 5/3$ it acts adiabatically; thus

$$\beta \sim \frac{c_s^2}{c_A^2}$$

where upstream values are understood. The plasma beta (β) is an important parameter which indicates whether magnetic pressure dominates the plasma behavior ($\beta \ll 1$) or whether thermal effects are important ($\beta \geq 1$). Low β plasmas can often be considered to be cold plasmas ($T \sim 0$) with particle thermal motion ignored. In high β plasmas ($\beta \sim 1$) the thermal motions cannot be ignored because the interactions of waves and particles leads to plasma behavior (such as wave damping and growth) not found in cold plasmas.

Another parameter often used to classify shocks is the shock normal angle, $\psi(\vec{B}, \hat{n})$, the angle between the upstream magnetic field and the shock normal. Perpendicular and parallel shocks have shock normal angles of 90° and 0° , respectively. Oblique shocks have intermediate angles. From (13) we can see that the normal component of magnetic field is conserved through a shock; thus changes in magnitude and direction occur only in the tangential component. If a shock is a perpendicular shock, ($\vec{B} \cdot \hat{n} = 0$) the only changes in the magnetic field are in its magnitude, the direction remaining constant.

For the case of the earth's bow shock, appropriate values of the shock parameters are $\beta \sim 1$, $M_A \sim 5$ and $\psi(\vec{B}, \hat{n}) \sim 30^\circ - 70^\circ$. The bow shock is thus, on the average, a high beta, high Mach number, oblique shock.

The validity of the MHD equations (1) - (4) requires that fluid properties be retained over appropriate length and time scales. This means that the isotropy of the charged particle distributions must

be attained over lengths and times smaller than the scale lengths and times that characterize the flow. In other words the mean free path for collisions λ_c and the collision frequency ν_c must satisfy $\lambda_c \ll \lambda_s$ and $\nu_c \gg \omega_s$, where λ_s and ω_s are length and frequency scales for the flow. These requirements are implicit in the assumption of an adiabatic equation of state for the plasma, as in equation (4). Now the three elementary wave modes of the MHD fluid have no basic scale length, i.e., all wavelengths of a given mode have the same phase velocity. For shocks, however, a basic scale length is required, the shock thickness L_s over which the gradients of plasma properties are appreciable. This indicates that the model of the idealized MHD fluid, equations (1) - (4), cannot be correct for shocks, even if the plasma otherwise satisfies the requirements for fluid flow. In the presence of a zero-order magnetic field the requirements for fluid flow may be relaxed somewhat to $\lambda_c \ll r_i$ and $\nu_c \gg \Omega_e$ where r_i is the ion gyroradius and Ω_e is the electron gyrofrequency. These inequalities mean that isotropy is maintained in directions perpendicular to the magnetic field independently of the parallel direction. The adiabatic equation of state may now be replaced by two adiabatic equations, for $P_{||}$ and P_{\perp} . This introduces an anisotropy into the fluid equations and may be expected to result in modifications of the elementary wave modes and the resulting shock jump conditions.

One model of anisotropic pressure which has been used are the CGL equations [Chew, Goldberger, and Low, 1956]:

$$\frac{D}{Dt} \left(\frac{P}{\rho B} \right) = 0 \quad (14)$$

$$\frac{D}{Dt} \left(\frac{P_{\parallel} B^2}{3\rho} \right) = 0 \quad (15)$$

where $\frac{D}{Dt} = \frac{\partial}{\partial t} + \vec{v} \cdot \nabla$. These equations express conservation of the magnetic moment $\mu = 1/2 m v_{\perp}^2 / B$ and zero parallel heat flow, respectively. The CGL equations are appropriate in low β plasmas, and less accurate for $\beta \sim 1$.

B. The Two-Fluid Plasma

For a collisionless, magnetized plasma like the solar wind the requirements for fluid flow are not met ($\lambda_c \gg \lambda_s$, $\lambda_c \sim 1$ AU) and it would appear that the fluid equations do not apply. However, experimental measurements have shown that the equations do predict correct values for measurable quantities over large enough scale lengths. The position and flow characteristics of the bow shock and magnetosheath have been well described using the MHD equations [Spreiter et al., 1966; Formisano et al., 1973a] and the jump conditions have been successfully applied to the bow shock [Mihalov et al., 1969; Formisano et al., 1973b]. The resolution of this apparent paradox lies in the long range Coulomb force between the charged particles in the solar wind. The Coulomb interaction serves to weakly bind the electron and ion gases and, along with the magnetic field,

provides a coherence to the flow necessary for the fluid approximation. Over large enough scale lengths, the solar wind therefore appears to be a single fluid. On smaller scales, however, measurements (near the earth) show that the electron and proton gases have different temperatures ($T_e \sim 10^5 \text{K}$, $T_p \sim 5 \times 10^4 \text{K}$) in addition to having anisotropic pressure (P_\perp , P_\parallel). These temperatures and pressures arise from the lack of binary collisions, which prevents the electron and proton gases from acting together as one fluid, with one temperature and pressure. As a result, the solar wind is more like a two-fluid, anisotropic plasma with particle distributions given by bi-Maxwellians for both electrons and protons [Hundhausen, 1968, 1970]. The electron anisotropy is small and can be ignored, but for protons it results in temperatures $T_{p\parallel} = 4 \times 10^4 \text{K}$ and $T_{p\perp} = 2 \times 10^4 \text{K}$.

A more accurate description of the solar wind thus requires that fluid equations be used for the electron and proton gases separately, with terms included for the Coulomb interaction between the gases. The Coulomb interaction could be represented by an 'effective' collision frequency, for which a value 10 times greater than the classical binary collision frequency is found to explain the electron and proton temperatures at 1 AU [Nishida, 1969]. The need for a larger effective collision frequency suggests that a possible approach to the two-fluid description of the solar wind is to modify the assumption of infinite conductivity in Ohm's law used in the MHD approximation (equation (3) is obtained from Maxwell's equation using $\vec{E} + 1/c(\vec{v} \times \vec{B}) = \vec{J}/\sigma \rightarrow 0$). The resulting elementary wave modes of

the two-fluid plasma may then be expected to be dispersive (i.e., to have basic scale lengths) introduced by the effects of finite particle inertia. An attempt may then be made to relate the dissipative scale length of shocks, the shock thickness L_s , to the wave lengths of the possible wave modes, and thereby gain understanding of the dissipative processes themselves. However, various theoretical investigations [Tidman and Krall, 1971; Biskamp, 1973] show that below a critical Mach number $M_A^* \sim 2$ the shock thickness is determined by wave dispersion and above $M_A^* \sim 2$ dissipation determines the shock thickness. (This provides another categorization for shocks, laminar for $M_A < M_A^*$, turbulent for $M_A > M_A^*$.) The two possible scale lengths may not be totally independent so that for the earth's bow shock ($M_A \sim 5$) the shock thickness may involve both dispersive and dissipative scale lengths; a double structure may also exist in the transition [Paul et al., 1965, Woods, 1971].

In the two-fluid description, the mass conservation equation (1) remains unchanged in form when applied to each fluid separately. The momentum equation (2) must now include a source term on the right hand side, of opposite sign for each gas, to account for the transfer of momentum between the two fluids. These equations for the two fluids may therefore be added to regain mass and momentum conservation equations in the same form as for the one-fluid description, provided that the pressure terms for each gas are also of the same form. According to the assumptions made for the equation of state and/or Ohm's law the rest of the two-fluid equations take different

forms. One choice [Abraham-Shrauner, 1967a, 1968, 1973] that has been made is to use the CGL equations of state (14) and (15) and retain the assumption of infinite conductivity in Ohm's law, $\vec{E} + 1/c(\vec{v} \times \vec{B}) = 0$. This choice introduces considerable modification of the MHD wave modes depicted in Figure 3. Instabilities peculiar to the CGL assumption are also possible, being associated with violation of the adiabatic invariance of the magnetic moment μ and the longitudinal invariant J . For shocks, this offers a possible dissipation mechanism. The jump conditions for anisotropic pressure [Abraham-Shrauner, 1967b] acquire an additional equation, representing the additional conservation equation in the CGL pressure tensor.

For the earth's bow shock, however, the CGL equations of state are hard to justify because that model requires a strong enough magnetic field (low β) so that a preferred direction is established. The solar wind β is of order 1 and thus it is not clear that the magnetic field will impose a preferred direction for thermal motion in the bow shock.

Another form [Formisano and Kennel, 1969] of the two-fluid equations is obtained by retaining the isotropic equation of state (4) with different polytropic indices γ_- and γ_+ for electrons and protons (with resultant total pressure $P = P_+ + P_-$) and modifying Ohm's law to include the effects of finite particle inertia. For the problem of shock dissipation, this approach has the advantage of allowing for the introduction of dissipation in a natural way (through Ohm's law). The Ohm's law equation obtained for the linearized two-fluid equations is (after some algebraic manipulation)

$$\vec{E}_1 + \frac{1}{c}(\vec{v}_1 \times \vec{B}_0) = \frac{c^2}{\omega_{p+}^2} \left(\frac{4\pi ne}{c^2} \right) \frac{\partial \vec{v}_1}{\partial t} + \frac{c^2}{\omega_{p-}^2} \left(\frac{4\pi n}{c^2} \right) \frac{\partial \vec{J}}{\partial t} + \frac{\nabla P_{1+}}{ne} \quad (16)$$

where $\omega_{p\pm}^2 = \omega_{pi,e}^2 = 4\pi ne^2/m_{i,e}$ are the ion and electron plasma frequencies and P_{1+} is the partial pressure of ions. The first two terms on the right hand side represent the effects of particle inertia with characteristic inertial lengths c/ω_{p+} for ions and c/ω_{p-} for electrons. These characteristic lengths enter into the theory of plasma shocks [Tidman and Krall, 1971] where it is found that c/ω_{p-} and c/ω_{p+} are characteristic transition lengths for perpendicular and oblique shocks, respectively.

Assuming harmonic perturbations of the form $\vec{B}_1(x, t) = B_1 \hat{b} \exp i(\vec{k} \cdot \vec{x} - \omega t)$ in the linearized fluid equations, Formisano and Kennel [1969] obtain the dispersion relation

$$\begin{aligned} & (\cos^2 \theta - Q \frac{\omega^2}{k^2 C_A^2}) \left[(\cos^2 \theta - \frac{\omega^2}{k^2 C_s^2}) - Q \frac{\omega^2}{k^2 C_A^2} (1 - \frac{\omega^2}{k^2 C_s^2}) \right] \\ & = \frac{\omega^2 \cos^2 \theta}{\Omega_+^2} (1 - \frac{\omega^2}{k^2 C_s^2}) \end{aligned} \quad (17)$$

where θ is the angle between \vec{k} and \vec{B}_0 . The effect of ion inertia is represented by the ion gyrofrequency $\Omega_+ = \Omega_i = eB/m_i c$. Electron inertia is represented by $Q = 1 + k^2 c^2 / \omega_{p-}^2$. C_s and C_A are the sound and Alfvén velocities. The wave modes of the dispersion relation (17) are shown in Figure 4, where it may be seen that they

connect with the MHD fast, intermediate, and slow waves (also called the magnetosonic, Alfvén, and ion acoustic waves) for frequencies $\omega < \Omega_+$. The MHD dispersion relations (7) and (8) can be obtained from (17) by taking the limits $Q = 1$ and $\omega^2/\Omega_+^2 \sim 0$ with phase velocity $v = \omega/k$. For frequencies $\omega \sim \Omega_+$ the slow mode couples to the intermediate mode, becoming the electroacoustic (or ion sound) wave, and the fast mode becomes the whistler wave. In the range $\Omega_+ < \omega < \Omega_-$ only the whistler and ion sound waves exist. At $\omega \sim \Omega_-$ the whistler and the ion sound waves couple so that only the ion sound wave remains above Ω_- .

Of particular interest are the whistler and ion sound branches in the range $10^0 < \omega/\Omega_+ < 2 \times 10^3$. In this range the ion sound wave is given approximately by $\omega/k \approx C_s = [K(\gamma_- T_- + \gamma_+ T_+)/m_+]^{1/2}$, where the signs refer to electrons (-) and protons (+) and K is Boltzmann's constant. As the plasma temperature increases this branch moves toward the upper left hand corner of the plot so that intersections with the whistler branch occur. These intersections are mode coupling points (equal phase velocities) and energy in one mode can couple into the other mode. Thus, in the presence of a temperature gradient, as in the shock transition, a spectrum of mode coupling points may be expected to occur.

In Figure 5 is shown how the phase velocities of the two-fluid plasma wave modes depend on propagation angle θ and C_s^2/C_A^2 . The dotted circle in each diagram is a reference with radius equal to the value of C_s . Increasing temperature corresponds to increasing C_s^2/C_A^2 ($\sim \beta$).

Below $\omega/\Omega_+ = 10^0$ the three MHD modes corresponding to Figure 3 are to be found. For frequencies $10^0 < \omega/\Omega_+ < 2 \times 10^3$, only the whistler and ion sound waves exist. The diagonal for frequencies $\omega/\Omega_+ > 10^0$ represents the locus of coupling points between the ion sound and whistler waves for increasing temperature.

C. Plasma Wave Turbulence

We have previously stated that for the high Mach number shock, like the earth's bow shock, the dispersive properties of waves alone cannot provide the transition between the upstream and downstream states. Dissipation must be included to convert the streaming kinetic energy in the upstream region into thermal energy downstream. This can be done only by a broad spectrum of turbulent electric fields. Such turbulent transitions imply that unstably growing wave modes provide the Coulomb interactions that lead to an effective resistivity. The wave modes obtained with the fluid approximation for a plasma do not exhibit wave growth or damping because these are effects that depend on wave phase velocities becoming equal, or nearly equal, to some range of particle thermal velocities. In a fluid treatment, however, the particle thermal velocity distribution is replaced with an average fluid velocity, and the details of wave-particle interactions is lost; therefore the particle thermal velocity distribution must be considered.

Plasma instabilities generally fall into two classes: macroscopic, where the wave length of the unstable mode is of the same order as the scale length of the flow; and microscopic, for

which the wavelengths of unstable modes are much smaller than the scale lengths of the flow. Macroscopic instabilities are associated with the low frequency MHD wave modes while the microscopic instabilities occur at the higher characteristic frequencies of ions and electrons. For shock dissipation where particle distributions must be thermalized, the microscopic instabilities are the important sources of turbulent electric fields. The gradient of magnetic field in the main shock transition may be associated with a macroscopic instability, such as the steepening of a fast wave.

Microscopic plasma instabilities require a kinetic treatment in which the particle thermal velocities and the wave phase velocities define regions of wave-particle interactions which can lead to growing or damped waves. For a collisionless plasma the appropriate starting point for this description is the Vlasov equation

$$\frac{\partial f}{\partial t} + \vec{v} \cdot \nabla f + \frac{e}{m} \left(\vec{E} + \frac{\vec{v}}{c} \times \vec{B} \right) \cdot \nabla_{\vec{v}} f = 0 \quad (18)$$

where $f = f(\vec{x}, \vec{v}, t)$ is the distribution function for a given particle species and $\nabla_{\vec{v}} = \frac{\partial}{\partial \vec{v}}$. Maxwell's equations give the self-consistent fields.

The Vlasov-Maxwell system of equations is linearized by assuming that the distribution function $f(\vec{x}, \vec{v}, t)$ and the fields $\vec{E}(\vec{x}, t)$ and $\vec{B}(\vec{x}, t)$ can be written as the sum of average and perturbed quantities:

$$f = f_0 + f_1$$

$$\vec{E} = \vec{E}_0 + \vec{E}_1$$

$$\vec{B} = \vec{B}_0 + \vec{B}_1$$

and then solving for the perturbed quantities. When this is done, the resulting set of equations for each particle species is

$$\begin{aligned} \frac{\partial f_1}{\partial t} + \vec{v} \cdot \nabla f_1 + \frac{e}{m}(\vec{E}_0 + \frac{\vec{v}}{c} \times \vec{B}_0) \cdot \nabla_{\vec{v}} f_1 + \frac{e}{m}(\vec{E}_1 + \frac{\vec{v}}{c} \times \vec{B}_1) \cdot \nabla_{\vec{v}} f_0 \\ = - \frac{e}{m}(\vec{E}_1 + \frac{\vec{v}}{c} \times \vec{B}_1) \cdot \nabla_{\vec{v}} f_1 - C \end{aligned}$$

$$\nabla \cdot \vec{E}_1 = 4\pi \sum n e \int f_1 d\vec{v}$$

$$\nabla \times \vec{B}_1 = \frac{1}{c} \frac{\partial \vec{E}_1}{\partial t} + \frac{4\pi}{c} \sum n e \int f_1 \vec{v} d\vec{v}$$

$$\nabla \times \vec{E}_1 = - \frac{1}{c} \frac{\partial \vec{B}_1}{\partial t}$$

where an effective collision term $C = - \frac{e}{m} \left\langle (\vec{E}_1 + \frac{\vec{v}}{c} \times \vec{B}_1) \cdot \nabla_{\vec{v}} f_1 \right\rangle$

now exists which represents the interaction between particle distributions and fields that results in dissipative turbulence.

The wave modes of the plasma are obtained by considering only the first order terms of the Vlasov equation. An immediate simplification that can be made is the electrostatic approximation, i.e., the assumption that the electric field is derivable from a potential, $\vec{E}_1 = - \nabla \phi_1$, and that $\vec{B}_0 = \vec{B}_1 = 0$. Assuming also that f_1 and ϕ_1 vary as $\exp i(\vec{k} \cdot \vec{x} - \omega t)$, where $\omega = \omega_r + i\omega_i$ has real and imaginary

parts (to allow for damped or growing modes) the first order equations result in the complex dispersion relation

$$D(\vec{k}, \omega_r) = D_r(\vec{k}, \omega_r) + i D_i(\vec{k}, \omega_r)$$

which gives the wave dispersion relation

$$D_r(\vec{k}, \omega_r) = 0$$

and growth rate

$$\omega_i = - \frac{D_i(\vec{k}, \omega_r)}{\partial D_r(\vec{k}, \omega_r) / \partial \omega_r}, \quad \left| \frac{\omega_i}{\omega_r} \right| \ll 1$$

where $\omega_i \ll \omega_r$ is required for weakly damped waves to exist as elementary modes of oscillation for the plasma. The details of the derivation of these equations can be found in most plasma physics textbooks.

According to the limits assumed for the phase velocities, two modes of electrostatic oscillations ($\vec{E}_1 \parallel \vec{k}$) can be found for Maxwellian particle distributions, electron plasma oscillations and ion acoustic waves. The dispersion relations and growth rates for these modes are [Krall and Trivelpiece, 1973]:

a) electron plasma oscillations

$$\omega_r^2 = \omega_{pe}^2 \left(1 + \frac{3}{2} k^2 \lambda_D^2 \right) \quad (19)$$

$$\omega_i = \sqrt{\frac{\pi}{8}} \frac{\omega_{pe}}{|k^3 \lambda_D^3|} \exp - \left(\frac{1}{2k^2 \lambda_D^2} - \frac{3}{2} \right) \quad (20)$$

where $\omega/k \gg v_{\text{thermal}} = (KT_e/m_e)^{1/2}$ and $k\lambda_D \ll 1$ for weak damping.

b) ion acoustic waves

$$\omega_r^2 = \frac{k^2 C_s^2}{1+k^2 \lambda_D^2} \quad (21)$$

$$\omega_i = - \frac{|\omega_r| \sqrt{\pi/8}}{(1+k^2 \lambda_D^2)^{3/2}} \left\{ \left(\frac{T_e}{T_i} \right)^{3/2} \exp \left[- \frac{(T_e/T_i)}{2(1+k^2 \lambda_D^2)} \right] + \left(\frac{m_e}{m_i} \right)^{1/2} \right\} \quad (22)$$

where $\left(\frac{KT_i}{m_i} \right)^{1/2} < \frac{\omega}{k} < \left(\frac{KT_e}{m_e} \right)^{1/2}$

and $C_s^2 = \frac{KT_e}{m_i}$ is the sound speed.

The requirement $|\omega_i/\omega_r| \ll 1$ for weakly damped ion acoustic waves means $T_e \gg T_i$.

The dispersion relations (19) and (21) are obtained assuming there is no magnetic field, however the same equations hold in the presence of a magnetic field and represent electrostatic oscillations parallel to the magnetic field direction [Bernstein and Kulsrud, 1960].

An electrostatic mode also exists for waves propagating perpendicularly to the magnetic field [Bernstein, 1958; Stix, 1962].

These waves occur in narrow bands between harmonics of the electron

and ion gyrofrequencies and at the lower hybrid frequency $\Omega_{LH} = (\Omega_i \Omega_e)^{1/2}$ [Fredricks and Scarf, 1969]. These modes of propagation are referred to as the Bernstein modes and are strongly damped for directions of the wave vector \vec{k} a few degrees away from the perpendicular to the magnetic field.

The electrostatic modes discussed above are found to be unstably growing if a relative drift exists between two populations of charged particles and the drift velocity exceeds a certain level, usually at about the order of the wave phase velocity. Drifts arise from gradients of plasma variables and therefore the shock transition is expected to cause particle drifts due to gradients in magnetic field, density, temperature, etc.

For electrons drifting through ions with a drift velocity $v_D \sim C_s$ it has been found that ion sound waves grow unstably for $T_e \gg T_i$ [Fried and Gould, 1961]. The growth rate for ion sound waves when $v_D > C_s$ and for wavelengths $\lambda > \lambda_D$ is

$$\omega_i \sim -\omega_r \sqrt{\frac{\pi m_e}{8 m_i}} \left(1 - \frac{v_D}{C_s} \cos \theta\right) \quad (23)$$

where θ is the angle with respect to the drift velocity direction [Tidman and Krall, 1971]. Instability ($\omega_i > 0$) occurs for a wide range of angles of propagation about the direction of the drift velocity with Cerenkov cone angle $\cos \theta = \frac{C_s}{v_D}$.

For currents parallel to the magnetic field, drift waves associated with the self-consistent inhomogeneities generated by the currents can become unstable for $\omega \ll \Omega_i$ and $T_e \sim T_i$. As a result,

the critical electron streaming velocity for ion-wave current instability is much below the threshold of Fried and Gould [1961] for ion sound instability [Kan, 1971].

The wave instabilities discussed above can be applied to the discussion of electrostatic turbulence in plasma shocks. The shock model most often used in the discussion of shock turbulence is that of a perpendicular shock with diamagnetic current \vec{J} flowing across the magnetic field and in the plane of the shock front [Krall and Book, 1969]. The current is determined by $\vec{J} = c/4\pi(\nabla \times \vec{B}) = ne \vec{v}_D$, where \vec{v}_D is the net drift velocity in the gradients of magnetic field and density, $\epsilon = \nabla B/B$ and $\epsilon' = \nabla n/n$. For a model relevant to the earth's bow shock, it is assumed that $\omega_{pe} \gg \Omega_e$ and that the ions are 'unmagnetized', i.e., that $r_i(\nabla B/B) > 1$ so that ion trajectories are only slightly perturbed through the shock. For electrons, $r_e(\nabla B/B) \ll 1$ so that the diamagnetic current \vec{J} is an electron current. Several authors have refined the perpendicular shock model to include a steady electric field \vec{E} and a drift velocity from the temperature gradient $\delta = \nabla T/T$ [Biskamp, 1970; Gary and Sanderson, 1970; Priest and Sanderson, 1972]. The geometry of the model is depicted in Figure 6. For x increasing in the negative direction,

$$\vec{B} = B(1-\epsilon x)\hat{z}$$

$$n_e = n_e(1-\epsilon' x)$$

$$T_e = T_e(1-\delta x)$$

$$\vec{E} = E\hat{x}$$

with resultant drift velocities

$$\vec{v}_O = \frac{c}{B^2} \vec{E} \times \vec{B}$$

$$\vec{v}_n = \epsilon' \frac{v_e^2}{\Omega_e} \hat{y}$$

$$\vec{v}_T = \delta \frac{v_e^2}{\Omega_e} \hat{y}$$

where $v_e^2 = KT_e/m_e$. The net drift current is

$$\vec{J} = \epsilon \frac{Bc}{4\pi} \hat{y} = n_e e \vec{v}_D = n_e e (v_O - v_n - v_T) \hat{y}$$

For typical parameters in the earth's bow shock, the condition for unstably growing ion sound waves, $v_D > C_s$, easily occurs. Most theoretical and some laboratory results have regarded ion sound turbulence as the source of collisionless shock dissipation for electron heating [see Biskamp, 1973, for a review]. More recently, an instability arising from coupling between ion sound waves and Doppler-shifted electron Bernstein modes (due to the $\vec{E} \times \vec{B}$ drift of electrons) has been regarded as a source of shock turbulence [Gary and Sanderson, 1970; Gary, 1970, 1971, 1972; Wu and Fredricks, 1972]. This instability is usually referred to as an electron cyclotron drift instability. The growth rate for this instability is found to be greater than for the ion sound instability [Gary and Sanderson, 1970] and may therefore be a more likely source of turbulence. For the

electron cyclotron drift instability, in contrast to the ion sound instability, the propagation angle of the wave vector \vec{k} is restricted to a very narrow cone of angles perpendicular to the magnetic field.

From the two turbulence models above, the ion sound and electron cyclotron drift instabilities, the resulting electrostatic field is oriented perpendicularly to the magnetic field. However, as Biskamp [1970] has shown for shocks in which $\omega_{pi} \sim \Omega_e$ (approximately true for the earth's bow shock) two limiting cases can be obtained for the ion sound instability, $k_{||}/k_{\perp} \lesssim (m_e/m_i)^{1/2}$, i.e., waves propagating perpendicularly and obliquely to the magnetic field, with oblique propagation occupying the largest volume of \vec{k} -space. The limiting case $k_{||}/k_{\perp} > (m_e/m_i)^{1/2}$ thus corresponds to an electrostatic field with a component parallel to the magnetic field.

The electrostatic modes discussed above have the perturbation electric field parallel to the wave vector, $\vec{E}_1 \parallel \vec{k}$. Electromagnetic solutions to the dispersion relation $D_r(\vec{k}, \omega_r) = 0$ also exist when $\vec{B}_0 \neq 0$ for which $\vec{E}_1 \perp \vec{k}$. In the frequency range of interest, $\Omega_i < \omega < \Omega_e$, the electromagnetic mode is the whistler wave (see Figure 4), which has the dispersion relation [Stix, 1962]

$$\left(\frac{kc}{\omega}\right)^2 = 1 - \frac{\omega_{pe}^2}{\omega(\omega - \Omega_e \cos\theta)} \quad (24)$$

where $n^2 = (kc/\omega)^2$ is the index of refraction and θ is the angle of propagation with respect to the magnetic field \vec{B}_0 . Whistler waves can become unstable by interacting with thermal electrons at the

resonance cone angle $\cos \theta = (\omega + \vec{k} \cdot \vec{v}_e) / \Omega_e$. The possibility of whistler turbulence providing the dissipation for collisionless shocks with a magnetic field has been investigated by several authors [Kennel and Petschek, 1968; Patrick and Pugh, 1969]. In average solar wind velocities, whistler waves can stand in the flow at the earth's bow shock and thus provide a turbulent wave energy density for particle thermalization [Scarf, 1970].

The unstable electrostatic and electromagnetic wave modes that are predicted by plasma theory must eventually be limited by non-linear interactions that tend to quench the instability. If an external source and sink of energy are available, however, a stationary turbulent state can be maintained [Ichimaru and Nakano, 1968]. For the earth's bow shock, an external source of energy exists in the flow kinetic energy of the solar wind and a sink is available in the thermalization of the magnetosheath particle distributions. Thus a stationary spectrum of turbulent plasma waves is maintained in the bow shock which can be measured over time scales long compared with the growth times of the unstable plasma waves. With experimental measurement of the plasma wave spectrum, an attempt can then be made to identify distinct wave modes.

IV. PLASMA WAVE SPECTRA IN THE BOW SHOCK

A. General Characteristics

Figure 7 illustrates the electric and magnetic field intensities typically observed in a bow shock crossing with the IMP-6 plasma wave experiment. Average and peak electric and magnetic field amplitudes are shown as a function of Universal Time (UT) for seven channels of both spectrum analyzers. The average field amplitudes are indicated by vertical lines and the peak field amplitudes by dots. The constant level for the peak measurements in the 36 Hz and 120 Hz electric field channels is caused by the previously mentioned interference from the solar array. The spacecraft crosses the bow shock, passing from the magnetosheath into the solar wind, at about 1048 UT, as indicated by the sharp enhancement in the electric field strength at all frequencies below about 10.0 kHz. The electric field noise in the bow shock typically extends over a very broad frequency range, usually from 36.0 Hz, which is the lowest frequency measured, to greater than 10.0 kHz. In some cases electric field noise associated with the bow shock has been detected up to 56.2 kHz.

The regions upstream and downstream of the bow shock are distinguished by their correspondingly low and high levels of electric field noise. In the magnetosheath the peak electric field

spectral density in the 1.00 kHz and 3.11 kHz channels is typically about three orders of magnitude above the solar wind levels. In the solar wind the peak field strengths, and to a lesser extent the average field strengths, are strongly modulated at the lower frequencies by the solar array noise.

Immediately upstream of the bow shock a distinct enhancement is evident in the 31.1 kHz electric field strength from about 1048 UT to 1055 UT. This noise is primarily electrostatic since no comparable enhancement is evident in the 31.1 kHz magnetic field data, and is caused by electron plasma oscillations at the local electron plasma frequency $\omega_{pe}/2\pi$. Several accounts of electron plasma oscillations of this type, generated by electrons streaming into the solar wind from the bow shock, have been previously reported [Fredricks et al., 1968; Scarf et al., 1971; Fredricks et al., 1971, 1972]. Electron plasma oscillations upstream of the bow shock are observed on almost all shock crossings with IMP-6.

Figure 7 shows only a slight increase in the magnetic field intensities at the bow shock. In the solar wind, upstream of the bow shock, the magnetic field intensities are below the sensitivity threshold of the receiver in all except the lowest frequency channel. In the magnetosheath, downstream of the bow shock, magnetic field fluctuations are evident in all frequency channels below about 1.00 kHz. These fluctuations are usually most evident in the peak measurements, indicating that the fluctuations occur on a time scale much less than the 5.12 second time constant for the average

field strength measurements. Often, the magnetic field measurements in the magnetosheath indicate turbulence at only two or three intermediate frequencies (such as 120 Hz and 200 Hz). The magnetosheath noise starts abruptly at the bow shock. The magnetic field fluctuations at the shock are usually only slightly larger than in the magnetosheath.

Figure 8 shows a double crossing of the bow shock, the first at about 1251 UT and the second at about 1252 UT, caused by oscillatory motion of the shock structure. A clean separation of the upstream and downstream regions by the shock transition occurs in this example, with the upstream solar wind region between 1251 and 1252 UT. The magnetic field measurements from the GSFC magnetometer on IMP-6 show a clear jump in the magnetic field at each crossing from a steady upstream value, $B_1 \simeq 5 \gamma$, to a downstream value, $B_2 \simeq 20 \gamma$. The angle between the upstream field and the shock normal calculated from the model of Fairfield [1971] is $\psi(\vec{B}, \hat{n}) \simeq 92^\circ$ for both crossings [D. Fairfield, personal communication]. The bow shock in this case is, therefore, a perpendicular shock. Measurement of the upstream electron and ion distributions by the LASL plasma probe on IMP-6 gives the shock parameters $M_A = 6.0$, $\beta = 0.54$, and $T_e/T_i = 3.3$.

Electric and magnetic field spectral densities, $E^2(\omega)$ and $B^2(\omega)$, have been computed for 16 snapshots obtained for the second crossing of the shock shown in Figure 8. Each snapshot of data provides a complete electric and magnetic field spectrum for both

average and peak measurements. The electric field strength is determined by dividing the measured AC voltage at the antenna terminals by one half of the tip-to-tip length, ignoring any antenna impedance corrections. The computed electric field spectral densities for the average field strength measurements are shown in the three-dimensional plot in Figure 9. The time axis is at an oblique angle in this plot and successive spectra are 5.12 seconds apart. The time indicated at the bottom of the figure is the UT of the first snapshot. For ease of reference, each spectrum is labeled by a snapshot number. Figure 10 shows the corresponding magnetic field spectra for the same time interval.

Beginning with snapshot 1, Figure 9, strong electric field noise is present in the 16.5 kHz channel which steadily decreases in magnitude as the shock is approached. This noise is the previously mentioned electrostatic electron plasma oscillations associated with electrons streaming into the solar wind from the bow shock. Low frequency noise associated with the shock begins in snapshot 3 and steadily increases in intensity to a maximum in snapshot 7, by which time the electron plasma oscillations have disappeared. For the crossing at 1252 UT, the maximum r. m. s. electric field, E_{rms} , obtained by integrating across the entire frequency range, from 20 Hz to 200 kHz, occurs in snapshot 7 and has a value of 8.73×10^{-4} volts/m. Up to 98% of the contribution to E_{rms} comes from below 1 kHz and the spectrum has a broad maximum in the frequency range from about 200 Hz to 800 Hz. After the 7th snapshot, the low frequency noise decreases

in magnitude but the characteristic shape of the spectrum at the shock is maintained through the last snapshot in the figure. Examination of spectra taken when spacecraft is well into the downstream magnetosheath region on this and other crossings reveals that although there are variations in the low frequency portion of the spectrum the shape of the magnetosheath spectrum is the same as in the shock. Thus, the electric field spectrum in the shock appears to be carried into the downstream region. The downstream spectra also has a roughly periodic modulation of low frequency intensities with a period of about 4 snapshots, or about 20 seconds. This modulation appears to be a general feature of the downstream electric field spectra near the bow shock. Modulation periods range up to 60-70 seconds.

The magnetic field spectra, Figure 10, reveal the shock transition as merely an enhancement of low frequency noise. Above about 3 kHz the spectral densities are close to or at the receiver noise level. The maximum r. m. s. magnetic field intensity, obtained by integrating across the entire frequency range, 20 Hz to 200 kHz, occurs in snapshot 6 and has a value of $5.49 \times 10^{-2} \text{ v}$. Most of the contribution to B_{rms} comes from below 100 Hz.

B. Electric and Magnetic Field Spectra in the Bow Shock

For purposes of surveying the electric and magnetic field spectra for a large number of shock crossings one spectrum must be selected which is representative of each shock crossing. The snapshot which gives the maximum r. m. s. field amplitude, using the

average spectral density measurements integrated from 20 Hz to 200 kHz, is selected as the shock spectrum. The electric and magnetic field spectra thus selected are denoted $E^2(\omega)_{sh}$ and $B^2(\omega)_{sh}$, and are referred to as the shock spectra.

A typical shock transition takes place over four or five snapshots, sometimes as many as ten. In the series of values of E_{rms} calculated for a given shock crossing, there is usually only one maximum in E_{rms} , thus clearly defining $E^2(\omega)_{sh}$. However, the series of values of B_{rms} calculated through the same shock crossing may have several maxima, none of which occurs at the same time as the maximum in E_{rms} . For these cases we choose as the shock magnetic field spectrum, $B^2(\omega)_{sh}$, that one which gives the largest value of B_{rms} within three snapshots of the shock electric field spectrum.

From the discussion above, it can be seen that the determination of the characteristic electric and magnetic fields shock spectra is based on the snapshot in which the most intense low frequency electric field noise occurs. It is considered that this is appropriate, since the shock transition would be characterized by the spectrum $E^2(\omega)_{sh}$ that represents the greatest dissipation, i.e., the one with greatest turbulent electric field energy density.

Figure 11 shows the shock electric field spectrum selected for the shock crossing at 1252 UT. This spectrum corresponds to snapshot 7 in Figure 9. Both the peak and average electric field strengths obtained during this snapshot are shown. The noise level indicated

in Figure 11 is the ambient noise level (both interference and natural noise) which existed in the solar wind just ahead of the shock. The shape of both the average and peak electric field spectrum is characteristic of all the shock spectra examined in this study. However, as will be shown, the intensities at a given frequency vary over two orders of magnitude. The inflection in the spectrum at about 200 Hz in Figure 11, sometimes becomes very pronounced so that a broad peak develops in the spectrum between 200 to 800 Hz. The existence of a distinct peak in the spectrum suggests that this component of the electric field noise (indicated by the dashed curve in Figure 11) may result from a discrete noise source in the wave spectrum which is broadened by Doppler shifts and non-linear interactions. The tendency for the electric field spectral density to continue to increase with decreasing frequency below about 100 Hz suggests that a second component also exists in the electric field spectrum varying approximately as f^{-2} (straight dashed line in Figure 11).

The electric field spectrum from the peak measurements in Figure 11 is from the same 5.12 second averaging period as the average measurements. The peak spectrum has approximately the same shape as the average spectrum but is shifted upward in intensity by about an order of magnitude. The large ratio between the peak and average measurements indicates that the field strength has large (order of magnitude) fluctuations on a time scale less than the averaging time (5.12 seconds). The peak measurements give the upper bound on these

fluctuations. For many shocks the peak spectrum does not have a smooth shape like the average spectrum but has a more irregular appearance with several sharp maxima. Most of these sharp maxima are grouped around two frequencies: one near the local electron plasma frequency in the upstream solar wind, and the other near the broad peak in the average shock electric field spectrum.

Figure 12 shows the shock magnetic field spectrum selected for the shock crossing at 1252 UT in Figure 8. This spectrum corresponds to snapshot 6 in Figure 10, however, in accordance with the selection criterion this shock spectrum does not correspond in time with the shock electric field spectrum since in this case the maximum r. m. s. magnetic field intensity occurred slightly before (upstream of) the maximum r. m. s. electric field intensity. Both the average and peak magnetic field spectra exhibit a generally smooth monotonic decrease with increasing frequency, varying approximately as f^{-4} in the range from 20 Hz to 200 Hz, with no evidence of a peak in the spectrum comparable to the peak in the electric field spectrum. A distinct steepening of the spectrum is also evident at a frequency of about 200 Hz. This steepening of the spectrum occurs at a frequency slightly below the local electron gyrofrequency, which in this case is about 350 Hz. The peak magnetic field spectral density is about an order of magnitude greater than the average magnetic field spectral density indicating the presence of large fluctuations on a time scale less than 5.12 seconds.

In Figure 13 the peak and average electric field spectra, $E^2(\omega)_{sh}$, for 36 shock crossings selected at random from the IMP-6 data are overlaid to illustrate the range and variability of the electric field spectrum in the shock. In the majority of cases these spectra exhibit the same spectral shape illustrated in Figure 11. Two distinct components are evident in the average electric field spectra, and to a lesser extent in the peak spectra: one component, at low frequencies, decreases monotonically with increasing frequency approximately as $f^{-(2.0 \pm 0.5)}$, and the other component has a broad peak centered between 200 Hz to 800 Hz. The greatest variation in the spectral shape appears to occur in the spectra with the lowest intensities, ranging from spectra which decrease monotonically with no evidence of a peak, to spectra which have a distinct peak which is displaced toward higher frequencies (~ 3 kHz). The largest intensity variation, which occurs in the range from about 200 Hz to 3 kHz, is associated with the broad peak in the spectrum. As the electric field intensity increases starting from the lowest level, the peak initially becomes more pronounced until at an intermediate level the intensity of the monotonic component starts to increase and gradually merges with the broad peak. Except for the lowest intensities, the main contribution to the r. m. s. electric field strength comes from the peak. As will be shown, the broad peak in the spectrum is caused by electrostatic turbulence and the monotonic component is caused by electromagnetic whistler mode turbulence. In this study the largest r. m. s. electric field strength

encountered from the peak measurements is 2.3×10^{-2} volts m^{-1} . The largest r. m. s. electric field strength from the average measurements is 6.6×10^{-3} volts m^{-1} .

Figure 14 shows the overlayed peak and average magnetic field spectra for the same 36 shock crossings used in Figure 13. These spectra tend to show a monotonic decrease with increasing frequency, varying approximately as $f^{-(4.0 \pm 0.5)}$ in the range from about 30 Hz to 100 Hz with clear evidence of a steepening in the spectrum at about 100 to 200 Hz. This steepening in the magnetic field spectrum usually occurs slightly below the local electron gyrofrequency.

C. Electric to Magnetic Energy Density Ratio

To aid in identifying the plasma wave modes involved in the bow shock turbulence the electric to magnetic field energy density ratio can be calculated as the spacecraft passes through a shock. Figure 15 shows the ratio of simultaneously measured energy densities, $(E^2/8\pi)/(B^2/8\pi)$, at a sequence of snapshots for the shock crossing at 1252 UT in Figure 8. The snapshot numbers refer to the spectra of Figures 9 and 10. Because the magnetic field intensities at high frequencies (> 3 kHz) are often comparable to, or less than, the receiver noise level, the magnetic energy densities must be corrected for the receiver noise level. Only magnetic field measurements which exceed the receiver noise level by at least two quantizing steps (0.8 db) are used. At frequencies greater than about 10 kHz the magnetic field intensity is usually too small to be accurately measured so the energy density ratio cannot be determined at these

high frequencies. As the spacecraft passes through the shock a prominent peak develops in the energy density ratio at about 1 kHz. At snapshot 7, which is the time at which the most intense r. m. s. electric field occurs (see Figure 9) the maximum energy density ratio is $(E^2/8\pi)/(B^2/8\pi) \simeq 5 \times 10^2$. This large ratio coincides in frequency with the broad peak in the electric field spectrum and indicates that this component of the spectrum consists of almost purely electrostatic waves.

Considering the lower frequency limit of the electrostatic turbulence to be given by the frequency where $(E^2/8\pi)/(B^2/8\pi) = 1$ (indicated by the dashed line in Figure 15) then it is seen that the electrostatic noise broadens toward lower frequencies as the electric field intensity increases. There is thus an indication that as the shock is traversed from the upstream to the downstream sides, the electrostatic turbulence first begins at high frequencies and then spreads toward lower frequencies further into the transition region, where the main shock dissipation occurs. Only the increase to maximum intensity is shown in Figure 15, the decrease to the downstream state having approximately similar curves. At frequencies below about 120 Hz the energy density ratio remains approximately constant through the transition region, as in snapshots 5, 6, and 7, indicating that at these frequencies the shock turbulence involves a distinct electromagnetic mode.

To indicate the range and distribution of electric and magnetic energy density ratios in the bow shock Figure 16 shows an overlay

of the energy density ratio for 10 shock crossings selected at random. The simultaneous electric and magnetic field energy spectra used to calculate these ratios were selected on the basis of the maximum r. m. s. electric field intensity obtained from the average measurements. The energy density ratios for the shock crossings selected in Figure 16 show the same basic features evident for the single shock crossing in Figure 15. In the frequency range above about 200 Hz the electric field energy density exceeds the magnetic field energy density, sometimes by a factor of as much as 10^4 , confirming that the broad peak in the electric field spectrum consists of almost purely electrostatic waves. At frequencies below about 200 Hz the spectra with the lowest energy density ratio, in the range from 10^{-3} to 10^{-4} , show a distinct change in the slope, similar to snapshots 5, 6, and 7 in Figure 15. These energy density ratios correspond to the low frequency monotonic components of the electric and magnetic field spectra. In this frequency range (between the ion and electron gyrofrequencies) the only electromagnetic wave which can propagate is in the whistler mode (see Figure 4). The observed energy density ratios, 10^{-3} to 10^{-4} , are consistent with the electric to magnetic field ratio expected for whistler mode waves. The tendency for the energy density ratio to increase with increasing frequency, approximately proportional to $f^{1.5 \pm 0.5}$, is also consistent with the expected variation of the whistler mode refractive index, hence electric to magnetic field ratio, in this frequency range. The steepening of the

magnetic field spectrum at $f \simeq 200$ Hz, evident in Figures 12 and 14, can be attributed to the whistler mode propagation cutoff at the local electron gyrofrequency. On the basis of this evidence we conclude that the low frequency monotonic components of the electric and magnetic field spectra is caused by whistler mode turbulence generated in the bow shock.

D. High Resolution Spectra

Wideband analog spectra of the shock crossings at 1251 and 1252 UT in Figure 8 are shown in Figure 17 for the range 0 to 500 Hz. The quiet upstream and turbulent downstream regions are clearly evident in the electric field spectrum. The shock transition region is most evident in the magnetic spectrum. Both the electric and magnetic field spectra show a relatively unstructured noise enhancement in the shock transition. In the downstream region the electric field spectrum shows many 2 to 3 second bursts which have a distinct 'parabolic' frequency-time structure, sweeping rapidly downward in frequency from about 800 Hz, reaching a minimum of about 50 Hz, and then rapidly sweeping back upward in frequency. These bursts are almost purely electrostatic since no associated magnetic field is detected. They occur randomly in time and are characteristic of the downstream magnetosheath electric field spectrum. The distinctive frequency-time structure of these noise bursts has never previously been reported and this electrostatic noise appears to represent a basic new turbulence dissipation mechanism operative in the magnetosheath. The time scale of these bursts is not

resolved by the 5.12 second averages measurements in the digital data of Figure 8, however, the peak measurements are indicative of the peak amplitude of the bursts.

An expanded time scale spectrogram of the shock crossing at 1252 UT is shown in Figure 18, for frequencies up to 1 kHz. The low frequency electric field turbulence in the shock can be seen between 1252:10 and 1252:15 UT, corresponding to the time interval of snapshot 7, Figure 11. The intense, broadband electric field noise in the shock is clearly distinguished from the downstream region (after 1252:15 UT) in which a few 'parabola-shaped' bursts are intermingled with the background noise. The most intense portion of the low frequency magnetic noise occurs between 1252:00 and 1252:10 UT (corresponding to snapshot 6 of Figure 10), slightly upstream of the point where the most intense electric field noise occurs.

V. ELECTRIC FIELD POLARIZATION

From previous discussion it can be seen that for electrostatic waves the direction of the electric field is in the same direction as the waves propagate, as indicated by the wave vector \vec{k} . Therefore, the orientation, or polarization, of the electric field with respect to the static magnetic field shows the direction of wave propagation with respect to the static magnetic field. Determining the wave electric field direction relative to the static magnetic field is of importance as an aid to identifying specific wave modes. The wave electric field direction, projected onto the plane of rotation of the electric antenna, can be determined from the modulation of the measured electric field amplitude due to the antenna rotation. A null in the measured electric field amplitude occurs when the antenna axis is perpendicular to the electric field direction and a maximum occurs when the antenna axis is parallel to the electric field direction. Since angular resolution measurements are required the rapid-sample data must be used for this type of analysis.

This method of determining the electric field direction relies on the noise intensity remaining nearly constant during at least one rotation (~ 11.1 seconds). For the upstream and downstream waves, which often have an approximately constant amplitude for many rotations, the electric field direction can be reliably determined

using this technique. Because the time required to traverse the bow shock is often comparable to the rotation period, it is more difficult to apply this technique to the noise which occurs in the shock. Only shock crossings which have an approximately constant amplitude for at least 10 seconds, or more can be analyzed. The number of cases which can be analyzed is further restricted by the automatic cycling of the rapid-sample mode which must coincidentally sample the correct electric field channel at the time the event of interest is encountered.

A. Upstream Electron Plasma Oscillations

Figure 19 shows an example of upstream electron plasma oscillations for which suitable rapid-sample measurements are available to determine the electric field direction. The electron plasma frequency in this case is estimated to be about 20 kHz. The spectrum of the plasma oscillations is sufficiently broad that moderate electric field intensities are evident in the 31.1 kHz channel throughout the entire region prior to the shock crossing at 1548:30 UT. The electrostatic noise labeled 'precursor' at 3.11 kHz appears to be a component of the electron plasma oscillation spectrum which has broadened to frequencies well below the local electron plasma frequency about 5 minutes before the shock is encountered. Precursor effects of this type are frequently observed in association with the bow shock, usually starting a few minutes before the shock is encountered.

Two periods, labeled A and B, are shown in Figure 19 during which rapid-sample measurements were obtained. The spin modulation of the electron plasma oscillations in the 31.1 kHz channel, starting at 1541:29 UT, is shown in the polar plot labeled A in Figure 19. The points shown in this polar plot are the electric field strengths obtained during the rapid-sample interval, plotted radially outward from the origin according to the logarithmic scale shown below the plot. The polar angle is the angle between the electric antenna axis and the satellite-sun line, measured counter clockwise as viewed from the north ecliptic pole (the spacecraft spin axis is perpendicular to the ecliptic plane). The static magnetic field direction, projected onto the ecliptic plane, is indicated by the dashed line in the polar plot, at an angle of $\phi_B = 94^\circ$. The total magnetic field vector lies above the ecliptic plane at an angle $\theta_B = 16^\circ$.

The points shown in the polar plot include four complete rotations of the spacecraft. The electric field intensities have a pronounced maximum when the antenna axis is parallel to the projected magnetic field direction and a minimum when the antenna axis is perpendicular to the magnetic field. Since the magnetic field direction in this case is very close to the plane of rotation of the electric antenna (the ecliptic plane) it is evident that the electric field direction of the upstream electron plasma oscillations is parallel to the static magnetic field, as would be expected if these waves are excited by electrons streaming along the static magnetic field. Polar plot B in Figure 19 shows that the electric field direction of

the precursor waves is also aligned parallel to the static magnetic field. Similar observations for other shock crossings with widely varying magnetic field directions shows that the electric field direction of these upstream electron plasma oscillations is always parallel to the static magnetic field.

B. Electrostatic Waves in the Bow Shock

A shock crossing for which the rapid-sample measurements were available in the transition region is shown in Figure 20. The shock crossing in this case occurred near the ecliptic plane at 10.3 hours local time with very quiet upstream conditions. The detailed electric field amplitude obtained from the rapid-sample data in the 3.11 kHz electric field channel is shown as a function of time in the upper left panel of Figure 20 with the GSFC magnetometer measurements of the static magnetic field for the same shock crossing shown in the lower left panel. The GSFC magnetometer shows that the upstream magnetic field direction is very nearly perpendicular to the shock normal, $\psi(\vec{B}, \hat{n}) \simeq 87^\circ$, so that the bow shock is a perpendicular shock. The IASL plasma probe measurements give shock parameters $M_A = 4.8$, $\beta = 0.28$, and $T_e/T_i = 6.7$. The electrostatic turbulence associated with the shock transition occurs between about 1440:37 to 1440:49 UT (the interval between labels a and b). In this same time interval the GSFC magnetometer data shows that the magnetic field has many short period, small amplitude fluctuations about an average field magnitude which increases monotonically from about 12γ to about 50γ . As shown by the vertical dashed lines the electrostatic noise of the

shock transition correlates closely with the initial gradient of the static magnetic field, a clear indication that the electrostatic noise is caused by a current-driven instability.

The electrostatic noise associated with the shock is near maximum intensity for one complete rotation so that a definite spin modulation pattern can be obtained. Since the bow shock is a perpendicular shock the magnetic field direction remains constant through the transition with direction angles of approximately $\phi_B = 255^\circ$ and $\theta_B = 43^\circ$. The magnetic field direction, projected onto the plane of rotation of the electric antenna, is indicated by the dashed line in the polar plot in the upper right corner of Figure 20.

The angular distribution of electric field strengths in the shock transition is seen to be symmetrically distributed with respect to the magnetic field direction, with two distinct maximums when the antenna axis is parallel to the projected magnetic field direction and a minimum when the antenna axis is perpendicular to the static magnetic field. Since only one rotation occurs in the region where the intense electrostatic noise occurs it is possible that this apparent spin modulation may be due to a coincidental variation of the noise intensity rather than a spin modulation effect. However, the magnetic field gradient, which is correlated with the electrostatic noise intensity, increases smoothly as the magnetic field magnitude reaches a single maximum and does not indicate a variation associated with the two electric field maximums (at about 1440:40 UT and 1440:46 UT) which occur when the antenna axis is parallel to the

magnetic field. Thus, it is felt that the angular distribution in the polar plot of Figure 20 is representative of the actual distribution of electric field directions in the shock. Since the magnetic field in this case has an appreciable component perpendicular to the plane of rotation of the electric antenna ($\theta_B = 43^\circ$) it cannot be definitely established that the electric field is aligned parallel to the magnetic field vector, although this is certainly the simplest and most obvious interpretation of the observed modulation. Other similar cases which have been examined usually show definite evidence of spin modulation, however never as pronounced as for the upstream plasma oscillations. The modulation factor is usually less than 2:1 for maximum and minimum amplitudes which indicates that wave vector directions of the electrostatic waves in the bow shock are distributed over a relatively broad range of angles. When a definite spin modulation is evident, as in Figure 20, the maximum electric field amplitude in the shock usually tends to occur in a direction parallel to the static magnetic field.

The downstream electric field measurements, after about 1440:50 UT, contains a series of sharply peaked fluctuations which display an exponentially decaying envelope, an indication that shock generated turbulence is damping to the less intense noise levels of the magnetosheath. Each of the sharply peaked fluctuations is correlated with gradients in the magnitude of the downstream static magnetic field.

The middle and lower right polar plots show the distribution of electric field directions for the downstream fluctuations. These fluctuations clearly do not show spin modulation effects associated with the rotation of the antenna in a steady electric field. It is therefore concluded that the downstream fluctuations are real variations of the downstream electric field with about a 3 second periodicity in the spacecraft frame. The direction angles ϕ_B and θ_B of the downstream magnetic field show an oscillation of the direction of the magnetic field vector that also has a 3 second periodicity. The sharply peaked electrostatic fluctuations appear to also be correlated with the maximum rates of change of the direction of the magnetic field vector.

C. Electrostatic Turbulence in the Magnetosheath

As previously discussed, a moderate level of electrostatic turbulence is always present in the magnetosheath downstream of the shock. Since the intensity of the magnetosheath electric field noise is usually relatively steady for several rotations of the spacecraft, the electric field direction can be determined with a high degree of confidence in this region. Figure 21 shows the polar plot of a series of rapid-sample measurements obtained in the magnetosheath about one minute after the shock crossing at 1612:20 UT. For this crossing, the bow shock parameters are $M_A = 1.8$, $\beta = 0.03$, $T_e/T_i = 4.0$, and $\psi(\vec{B}, \hat{n}) = 95^\circ$. These rapid-sample measurements are from the 3.11 kHz electric field channel and include four complete rotations of the spacecraft. The maximum electric field amplitude

again occurs when the electric antenna axis is oriented parallel to the static magnetic field direction (projected onto the ecliptic plane). The magnetic field vector in this case lies at an angle of $\theta_B = 35^\circ$ above the ecliptic plane. Other similar cases which have been analyzed show that the electric field direction of the magnetosheath turbulence is always oriented nearly parallel to the magnetic field direction. Usually the electric field amplitude perpendicular to the magnetic field is a factor of 3 to 5 below the amplitude parallel to the magnetic field, which indicates that the distribution of electric field directions is rather closely aligned with the static magnetic field direction (within 20° or less).

VI. INTENSITY VARIABILITY OF SHOCK TURBULENCE

A. Correlation with Upstream State

The variability of the spectral densities of plasma wave turbulence in the bow shock is illustrated in Figures 13 and 14. Since plasma wave shocks are usually categorized in terms of the upstream state through such parameters as M_A , β , T_e/T_i , and $\psi(\vec{B}, \hat{n})$, it is of interest to investigate the relationship between these parameters and the r. m. s. electric and magnetic field strengths measured in the bow shock. Using the least squares fitting technique, the linear correlation coefficients listed in Table 1 have been calculated for the upstream parameters indicated. $E_{rms,1}$ and $E_{rms,2}$ are the r. m. s. electric field strengths obtained from the average shock electric field spectrum by integrating from 20 Hz to 200 Hz, and from 200 Hz to 4 kHz, respectively. $E_{rms,1}$ and $E_{rms,2}$ are thus the r. m. s. field strengths of the electromagnetic and electrostatic components, respectively, of the shock electric field spectrum. B_{rms} is the r. m. s. magnetic field strength obtained by integrating the average shock magnetic field spectrum from 20 Hz to 200 kHz. For N points used in the least squares fit, R_c is the critical value of the correlation coefficient at the 1% level of significance for a two-parameter fit [Neville and Kennedy, 1964]. If the absolute value of the computed correlation coefficient $|R|$ exceeds R_c , the probability is 1% that

the observed correlation between the two parameters is due to chance alone. The two fitting equations shown in Table 1 have been used according to the range of magnitudes that occurred for the shock parameters. Since the measurements of electric and magnetic fields are taken with equal quantizing steps on a logarithmic scale, small field strength measurements have greater uncertainty. Therefore the points in the least squares fit are weighted accordingly [Bevington, 1969].

B. Electric Field Strength Dependence

A study of the coefficients in Table 1 reveals that the electric field strengths $E_{rms,1}$ and $E_{rms,2}$ are strongly correlated with several of the shock parameters. In particular, $E_{rms,2}$ and T_e/T_i have the largest value of R , indicating that a strong positive correlation exists between the intensity of electrostatic turbulence in the bow shock and the electron to ion temperature ratio in the upstream solar wind. Figure 22 shows the plot of $E_{rms,2}$ against T_e/T_i . The diagonal dashed line in Figure 22 is the line of regression for $E_{rms,2}$ on T_e/T_i , and the slope of this line indicates the apparent dependence of $E_{rms,2}$ on T_e/T_i . The large error bars are at $\pm \sigma(y)$, the standard deviation, above and below the line of regression and indicate the degree of dispersion of the data points about the mean. However, in this case the large dispersion does not mean that large random errors are present in the values of $E_{rms,2}$ since every point is definitely a shock measurement, for which $E_{rms,2}$ is at least an order of magnitude above the noise level. The dispersion of the

values of $E_{rms,2}$ is probably indicative of the dependence of $E_{rms,2}$ on other parameters besides T_e/T_i which are not included in the two-parameter fit. As is shown in Table 1, $E_{rms,2}$ displays strong correlation with other shock parameters, so that the total dependence of $E_{rms,2}$ is very likely a complex function of T_e/T_i , C_s , M_A , etc. The slope of the regression line is the important measure of association between $E_{rms,2}$ and T_e/T_i , and since the regression line is a mean fit, the standard deviation of the mean, $\sigma(\bar{y})$, is a better measure of dispersion because this tends to compensate for correlations not included in a two-parameter fit. The smaller error bars in Figure 22 are at the 1% level of significance, $\pm 2.576 \sigma(\bar{y})$. At their location on the regression line, the small error bars also indicate the 1% limits to the dispersion of the slope of the regression line about its midpoint. It is clear that the slope of the regression line does not change very much in these two limits. The points in Figure 22 also show that there appears to be a lower threshold for the electrostatic turbulence of the bow shock which moves toward higher intensities as T_e/T_i increases, as indicated by the solid diagonal line.

The association of $E_{rms,2}$ and the upstream sound speed C_s ($= [5/3K/m_i(T_e + T_i)]^{1/2}$) is shown in Figure 23, where the line of regression for the two-parameter fit is the diagonal dashed line and the error bars have the same meaning as in Figure 22. The slope of the regression line indicates that a significant negative correlation exists between electrostatic turbulence in the bow shock and the upstream sound speed.

Table 1 shows that $E_{rms,1}$, the electric field strength of the electromagnetic component of the shock spectrum, is best correlated with C_s . Figure 24 shows the plot of $E_{rms,1}$ against C_s . The slope of the line of regression indicates that a strong negative correlation exists between $E_{rms,1}$ and C_s , almost as strong as for $E_{rms,2}$ and C_s .

Table 1 also shows that for both electric and magnetic r. m. s. field strengths, no significant correlation is found with the shock normal angle, $\psi(\vec{B}, \hat{n})$.

C. Magnetic Field Turbulence

The r. m. s. magnetic field strength for the bow shock, B_{rms} , displays a substantially significant correlation only with $\psi(\vec{B}, \vec{V}_{SW})$, the angle between the upstream vectors of the static magnetic field and the solar wind velocity (see Table 1). Figure 25 shows the plot of B_{rms} and $\psi(\vec{B}, \vec{V}_{SW})$; the line of regression and error bars have the same meaning as in previous figures. The slope of the regression line indicates that more intense magnetic field turbulence occurs for larger values of $\psi(\vec{B}, \vec{V}_{SW})$. Since whistler waves propagate in a cone about the magnetic field direction, large angles $\psi(\vec{B}, \vec{V}_{SW})$ means that there will be less Doppler broadening of the wave spectrum by the solar wind. With a smaller volume of frequency space available for resonant interaction with the thermal particle distribution, less damping of the wave spectrum may result. The positive correlation between B_{rms} and $\psi(\vec{B}, \vec{V}_{SW})$ is then consistent with the previous conclusion that whistler waves comprise the shock magnetic field spectrum.

VII. SUMMARY OF RESULTS AND CONCLUSIONS

The plasma wave turbulence of the earth's bow shock has distinct electrostatic and electromagnetic components. The characteristic electric field spectrum of the bow shock shows that the electrostatic component has a broad peak centered at about 200 Hz to 800 Hz with a large electric to magnetic energy density ratio, $(E^2/8\pi)/(B^2/8\pi) \simeq 10^2$ to 10^4 , indicating almost purely electrostatic waves. Spin modulation measurements at the high frequency side of the broad peak (~ 3 kHz) show that the electric field direction of the electrostatic waves in the bow shock tends to be oriented parallel to the static magnetic field. Since usually only one rotation of the electric antennas is available in the shock transition this result is not as reliable as other spin modulation measurements where four complete rotations occur. However, a sufficient number of cases have been examined to be reasonably confident of the electric field orientation in the transition region. The maximum intensity of the electrostatic component of the shock electric field spectrum correlates closely with the initial gradient of the static magnetic field at the shock front, indicating that a current-driven instability is responsible for the electrostatic turbulence. The r. m. s. field strength of the electrostatic waves correlates positively with the upstream electron to ion temperature ratio, T_e/T_i , and negatively with the upstream sound velocity C_s (proportional to $(T_e + T_i)^{1/2}$).

The observed polarization of the electric field in the bow shock cannot be explained by any present theory. For the perpendicular shock of Figure 20 the electric field direction is determined to be oriented parallel to the static magnetic field, a result consistent with the electric field directions expected for ion sound waves propagating along the magnetic field direction [Biskamp, 1970; Tidman and Krall, 1971]. This electric field orientation is inconsistent with the perpendicular shock model of Krall and Book [1969] and with the electric field directions expected for the turbulent Bernstein wave mechanism suggested by Gary and Sanderson [1970], Wu and Fredricks [1972], and others.

The positive correlation between $E_{rms,2}$, the r. m. s. field strength for the electrostatic component of the shock electric field spectrum, and the temperature ratio T_e/T_i corresponds with the requirement for unstably growing ion sound waves and/or drift waves [Fried and Grould, 1961; Kan, 1971]. The negative correlation for $E_{rms,2}$ and the sound velocity C_s is also consistent with the requirement $v_D > C_s$ for unstable ion sound waves since an increasing value of C_s raises the threshold for instability.

The electrostatic component of the shock electric field spectrum almost certainly corresponds to the electrostatic waves discussed by Fredricks et al. [1968, 1970a, b] and Scarf et al. [1971] using electric field measurements from OGO-5. The electrostatic character of these waves, the general frequency range, and their occurrence in association with the magnetic field gradient at the shock transition

are in good agreement with the OGO-5 results. Detailed comparisons of the shape of the frequency spectrum are not possible since the OGO-5 data only provide measurements at a single frequency on a given shock crossing. The only area of disagreement concerns the electric field amplitude. Whereas Fredricks et al. quote electric field spectral densities at 1.3 kHz of 10^{-6} to 10^{-4} volts² m⁻² Hz⁻¹ (see discussion of Figure 4 on page 3757 of Fredricks et al. [1970b]), the largest peak electric field spectral density encountered by IMP-6 in this frequency range for the 150 shocks analyzed in this study is about 2×10^{-7} volts² m⁻² Hz⁻¹ (see Figure 13). This order of magnitude difference in the shock electric field amplitude has not been resolved. One possibility is that the wavelength of the electrostatic waves may be much shorter than the length of the long electric antennas on IMP-6. However, sufficiently short wavelengths (~ 10 meters) to account for such a large error would have a Doppler shift (~ 10 kHz) too large to account for the low frequency (200 to 800 Hz) at which the broad peak in the spectrum occurs. Also, comparisons between the two long antennas on IMP-6, which have different lengths, give consistent results and cross calibrations with the magnetic antennas, using electromagnetic waves with a known electric to magnetic field ratio, give consistent results [Gurnett and Shaw, 1973]. Further studies are being conducted using the short electric antenna on IMP-6, which is similar to the short electric antenna on OGO-5, to determine the reason for this apparent disagreement in the peak electric field amplitudes in the bow shock. (From a recent personal communication

with Scarf, the electric field amplitudes reported in Fredricks et al. [1970b] were too large due to a typographical error; peak electric field amplitudes obtained with OGO-5 are on the order of 30 millivolt/meter. Thus, OGO-5 electric field measurements are now only 1-3 times larger than IMP-6 measurements instead of an order of magnitude.)

The electromagnetic component of the shock electric field spectrum increases monotonically with decreasing frequency approximately as $f^{-(2.0 \pm 0.5)}$. Correspondingly, the shock magnetic field spectrum has only a single component which increases monotonically with decreasing frequency approximately as $f^{-(4.0 \pm 0.5)}$. The magnetic field spectrum also shows a distinct steepening of the spectrum, indicative of an upper cutoff frequency, at about 100 to 200 Hz. Since the whistler mode is the only electromagnetic mode which can propagate in this frequency range (above the proton gyrofrequency but below the electron gyrofrequency, see Figure 4) this magnetic field turbulence must be caused by whistler mode waves. The steepening of the magnetic field spectrum is thought to be associated with the whistler mode propagation cutoff at the local electron gyrofrequency, which is typically at about 350 Hz in the shock transition region. The monotonic component of the electric field spectrum is thought to be the electric field spectrum of these whistler mode waves. The electric to magnetic field energy density ratio, $(E^2/8\pi)/(B^2/8\pi) \simeq 10^{-3}$ to 10^{-4} of the monotonic component is consistent with the electric to magnetic field ratio expected for whistler mode waves. Also, the steeper magnetic field spectrum compared to the electric field spectrum is

expected for whistler waves because the index of refraction $n = cB/E$, hence magnetic to electric field ratio, increases with decreasing frequency, as indicated by equation (24). The negative correlation of the r. m. s. electric field strength $E_{rms,1}$ with the upstream sound velocity C_s is consistent with whistler waves because, as previously discussed, whistler waves may be expected to couple to ion sound waves, which have a similar correlation with C_s . The identification of whistler waves in the bow shock is also mutually consistent with ion sound waves because whistler waves propagate in a cone of wave vector directions oriented about the static magnetic field direction, similar to the observed electric field direction, hence wave vector direction, for electrostatic waves in the bow shock.

An interesting result of the association of bow shock turbulence with upstream parameters is the lack of a significant correlation with the shock normal angle $\psi(\vec{B}, \hat{n})$, so that both perpendicular and oblique shocks have similar spectra of plasma wave turbulence. This result may indicate that widely different properties for perpendicular and oblique shocks, i.e., the scale length of the transition region, do not occur.

Upstream of the bow shock intense narrow-band electrostatic plasma oscillations are frequently observed by the IMP-6 plasma wave experiment at frequencies of 10 kHz to 30 kHz. The spectrum and intensity of these electron plasma oscillations agree with the previous observations of Fredricks et al. [1968] and confirm the main features already known about these waves. The IMP-6 spin modulation measurements

show that the electric field vector of these plasma oscillations is oriented parallel to the local static magnetic field direction. This electric field direction is consistent with the direction expected if the plasma oscillations are produced by a two-stream instability from electrons which are streaming into the solar wind along magnetic field lines which intersect the shock transition. Broadband electrostatic noise, referred to as a precursor, is also frequently observed by IMP-6 immediately upstream of the shock. This broadband electrostatic noise typically extends from the local electron plasma frequency (which is usually at about 20 kHz to 30 kHz) down to frequencies of about 1 kHz. The electric field direction of these precursor waves is also oriented parallel to the static magnetic field. Since these precursor waves appear to be closely associated with the long wavelength narrow-band electron plasma oscillations (they have the same electric field polarization, and the upper frequency limit of the precursor spectrum is the local plasma frequency) it seems most likely that these waves are shorter wavelength electron plasma oscillations which are Doppler shifted downward in frequency from the local plasma frequency. A downward shift in frequency would be expected for waves propagating upstream into the solar wind.

In the magnetosheath, downstream of the bow shock, a moderate level of electrostatic turbulence is always present. This electrostatic turbulence has a spectrum similar to the electrostatic turbulence in the shock transition region, but with an electric field strength about one to two orders of magnitude smaller than in the

transition region. The spin-modulation measurements show that the electric field direction of this turbulence is also oriented parallel to the static magnetic field. The similarity of the spectrum and electric field direction of electrostatic turbulence in the bow shock and in the magnetosheath suggests that ion sound wave and/or drift wave turbulence also occurs in the downstream region with the lower intensity of the turbulence roughly proportional to the smaller magnetic field gradients which occur downstream.

LIST OF REFERENCES

- Abraham-Shrauner, B., Propagation of hydromagnetic waves through an anisotropic plasma, J. Plasma Phys., 1, 361, 1967a.
- Abraham-Shrauner, B., Shock jump conditions for an anisotropic plasma, J. Plasma Phys., 1, 379, 1967b.
- Abraham-Shrauner, B., Conservation equations for weakly turbulent plasmas, J. Geophys. Res., 73, 6299, 1968.
- Abraham-Shrauner, B., Small amplitude hydromagnetic waves for a plasma with a generalized polytrope law, Plasma Phys., 15, 375, 1973.
- Bernstein, I. B., Waves in a plasma in a magnetic field, Phy. Rev., 109, 10, 1958.
- Bernstein, I. B., and R. M. Kulsrud, Ion wave instabilities, Phys. Fluids, 3, 937, 1960.
- Bevington, P. R., Data Reduction and Error Analysis for the Physical Sciences, McGraw-Hill, New York, 1969.
- Biskamp, D., Ion sound turbulence in a collisionless shock wave, J. Geophys. Res., 75, 4659, 1970.
- Biskamp, D., Collisionless shock waves in plasmas, Nucl. Fusion, 13, 719, 1973.
- Chew, G. F., M. L. Goldberger, and F. E. Low, The Boltzmann equation and the one-fluid hydromagnetic equations in the absence of particle collisions, Proc. R. Soc. Lond., 236A, 112, 1956.
- Fairfield, D. H., Average and unusual locations of the earth's magnetopause and bow shock, J. Geophys. Res., 76, 6700, 1971.
- Formisano, V., and C. F. Kennel, Small amplitude waves in high β plasmas, J. Plasma Phys., 3, 55, 1969.
- Formisano, V., G. Moreno, and F. Palmiotto, Solar wind interaction with the earth's magnetic field, 1, Magnetosheath, J. Geophys. Res., 78, 3714, 1973a.

- Formisano, V., P. C. Hedgecock, G. Moreno, F. Palmiotto, and J. K. Chao, Solar wind interaction with the earth's magnetic field, 2, Magnetohydrodynamic bow shock, J. Geophys. Res., 78, 3731, 1973b.
- Formisano, V. and P. C. Hedgecock, Solar wind interaction with the earth's magnetic field, 3, On the earth's bow shock structure, J. Geophys. Res., 78, 3745, 1973a.
- Formisano, V. and P. C. Hedgecock, On the structure of the turbulent bow shock, J. Geophys. Res., 78, 6522, 1973b.
- Fredricks, R. W., C. F. Kennel, F. L. Scarf, G. M. Crook, and I. M. Green, Detection of electric-field turbulence in the earth's bow shock, Phys. Rev. Lett., 21, 1761, 1968.
- Fredricks, R. W. and F. L. Scarf, Electromagnetic and electrostatic Bernstein modes in a warm, collisionless Maxwell plasma, in Plasma Waves in Space and in the Laboratory, vol. 1, edited by J. O. Thomas and B. J. Landmark, p. 97, American Elsevier Publishing Company, 1969.
- Fredricks, R. W., F. V. Coroniti, C. F. Kennel, and F. L. Scarf, Fast time-resolved spectra of electrostatic turbulence in the earth's bow shock, Phys. Rev. Lett., 24, 994, 1970a.
- Fredricks, R. W., G. M. Crook, C. F. Kennel, I. M. Green, and F. L. Scarf,OGO 5 observations of electrostatic turbulence in bow shock magnetic structures, J. Geophys. Res., 75, 3751, 1970b.
- Fredricks, R. W. and F. L. Scarf, Nonthermal electrons and high-frequency waves in the upstream solar wind, 2, Analysis and interpretation, J. Geophys. Res., 76, 6691, 1971.
- Fredricks, R. W., F. L. Scarf, and I. M. Green, Distributions of electron plasma oscillations upstream from the earth's bow shock, J. Geophys. Res., 77, 1300, 1972.
- Fried, B. D., and R. W. Gould, Longitudinal ion oscillations in a hot plasma, Phys. Fluids, 4, 139, 1961.
- Gary, S. P., and J. J. Sanderson, Longitudinal waves in a perpendicular collisionless plasma shock, 1, Cold ions, J. Plasma Phys., 4, 739, 1970.
- Gary, S. P., Longitudinal waves in a perpendicular collisionless plasma shock, 2, Vlasov ions, J. Plasma Phys., 4, 753, 1970.

- Gary, S. P., Longitudinal waves in a perpendicular collisionless plasma shock, 3, $T_e \sim T_i$, J. Plasma Phys., 6, 561, 1971.
- Gary, S. P., Longitudinal waves in a perpendicular collisionless plasma shock, 4, Gradient B, J. Plasma Phys., 7, 417, 1972.
- Gurnett, D. A. and R. R. Shaw, Electromagnetic radiation trapped in the magnetosphere above the plasma frequency, J. Geophys. Res., 78, 8136, 1973.
- Holzer, R. E., M. G. McLeod, and E. J. Smith, Preliminary results from the OGO 1 search coil magnetometer: Boundary positions and magnetic noise spectra, J. Geophys. Res., 71, 1481, 1966.
- Holzer, R. E., T. G. Northrup, J. V. Olson, and C. T. Russell, Study of waves in the earth's bow shock, J. Geophys. Res., 77, 2264, 1972.
- Hundhausen, A. J., Direct observations of solar-wind particles, Space Sci. Rev., 8, 690, 1968.
- Hundhausen, A. J., Composition and dynamics of the solar wind plasma, Rev. Geophys. Space Phys., 8, 729, 1970.
- Ichimaru, S., and T. Nakano, Theory of a turbulent stationary state of a plasma, Phys. Rev., 165, 231, 1968.
- Jeffrey, A., Magnetohydrodynamics, Interscience Publishers, Inc., New York, 1966.
- Kan, J. R., Ion-wave current instabilities and anomalous resistivity, Phys. Fluids, 14, 2740, 1971.
- Kantrowitz, A. and H. E. Petschek, MHD characteristics and shock waves, in Plasma Physics in Theory and Application, edited by W. B. Kunkel, p. 147, McGraw-Hill, 1966.
- Kennel, C. F. and H. E. Petschek, Magnetic turbulence in shocks, Physics of the Magnetosphere, edited by R. L. Carovillano, D. Reidel Publishing Co., p. 485, 1968.
- Krall, N. A., and D. L. Book, Ion sound instability in a collisionless shock wave, Phys. Fluids, 12, 347, 1969.
- Krall, N. A. and A. W. Trivelpiece, Principles of Plasma Physics, McGraw-Hill, New York, 1973.
- Mihalov, J. D., C. P. Sonnett, and J. H. Wolfe, MHD Rankine-Hugoniot equations applied to earth's bow shock, J. Plasma Phys., 3, 449, 1969.

- Montgomery, M. D., J. R. Asbridge, and S. J. Bame, Vela 4 plasma observations near the earth's bow shock, J. Geophys. Res., 75, 1217, 1970.
- Neville, A. M. and J. B. Kennedy, Basic Statistical Methods, International Textbook Company, Scranton, Pennsylvania, 1964.
- Nishida, A., Thermal state and effective collision frequency in the solar wind plasma, J. Geophys. Res., 74, 5155, 1969.
- Olson, J. V., R. E. Holzer, and E. J. Smith, High-frequency magnetic fluctuations associated with the earth's bow shock, J. Geophys. Res., 74, 4601, 1969.
- Patrick, R. M., and E. R. Pugh, Laboratory study of turbulence in collision-free shocks, Phys. Fluids, 12, 366, 1969.
- Paul, J. W. M., L. S. Holmes, M. J. Parkinson, and J. Sheffield, Experimental observations on the structure of collisionless shock waves in a magnetized plasma, Nature, 208, 133, 1965.
- Priest, E. R., and J. J. Sanderson, Ion acoustic instability in collisionless shocks, Plasma Phys., 14, 951, 1972.
- Sanderson, J. J. and E. R. Priest, Perpendicular collisionless shock wave instability, Plasma Phys., 14, 959, 1972.
- Scarf, F. L. Microscopic structure of the solar wind, Space Sci. Rev., 11, 234, 1970.
- Scarf, F. L., R. W. Fredricks, L. A. Frank, and M. Neugebauer, Non-thermal electrons and high-frequency waves in the upstream solar wind, 1, Observations, J. Geophys. Res., 76, 5162, 1971.
- Spreiter, J. R., A. L. Summers, and A. Y. Alksne, Hydromagnetic flow around the magnetosphere, Planet. Space Sci., 14, 223, 1966.
- Stix, T. H., The Theory of Plasma Waves, McGraw-Hill, New York, 1962.
- Tidman, D. A., and N. A. Krall, Shock Waves in Collisionless Plasmas, John Wiley-Interscience, New York, 1971.
- Woods, L. C., On double-structured, perpendicular magneto-plasma shock waves, Plasma Phys., 13, 289, 1971.
- Wu, C. S. and R. W. Fredricks, Cyclotron drift instability in the bow shock, J. Geophys. Res., 77, 5585, 1972.

APPENDIX A: TABLES

TABLE 1
Linear Correlation Coefficient, R

$\begin{matrix} Y \\ X \end{matrix}$	$E_{rms, 1}$	$E_{rms, 2}$	B_{rms}	Regression Line
M_A	-0.333	-0.212	0.032	$\log y = a \log x + b$
β	-0.374	-0.268	-0.032	
T_e/T_i	0.368	0.554	-0.018	$\log y = a x + b$
C_s	-0.414	-0.489	-0.053	
V_{SW}	-0.191	-0.404	0.213	
$\psi(\vec{B}, \hat{n})$	-0.021	0.061	-0.017	
$\psi(\vec{B}, \vec{V}_{SW})$	0.259	0.300	0.291	
R_c	0.195	0.200	0.192	
N	178	158	179	

APPENDIX B: FIGURES

Figure 1 IMP-6 Spacecraft schematic.

D-G73-586-1

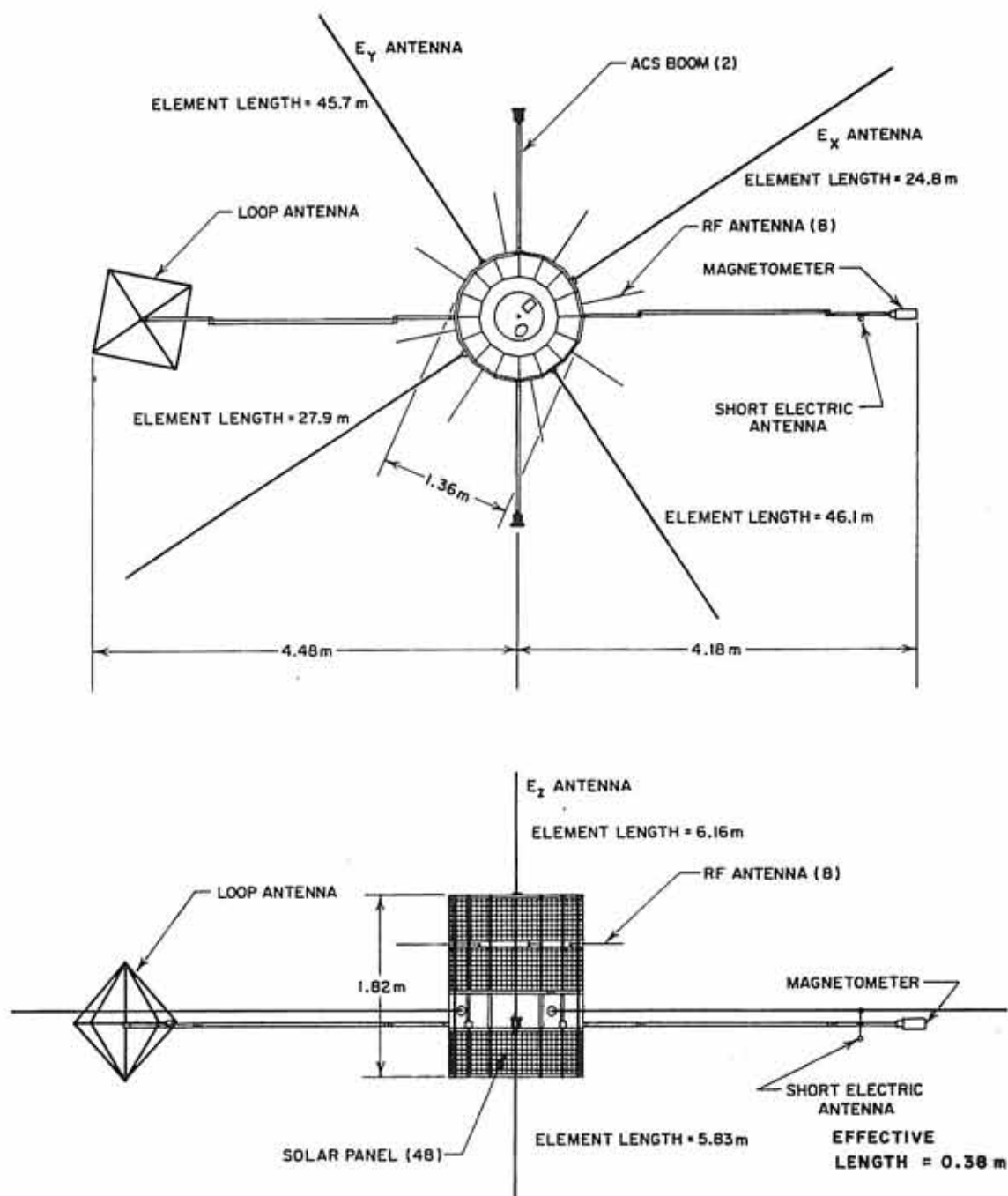


FIGURE 1

Figure 2 Block diagram of IMP-6 plasma wave experiment.

Figure 3 MHD wave modes. Polar plots showing the dependence of the propagation speeds of the three linear wave modes on the angle between the wave normal and the magnetic field for several values of the ratio of sound speed C_s to Alfven speed C_A . The speeds are normalized with respect to $(C_s^2 + C_A^2)^{1/2}$. [After Kantrowitz and Petschek, 1966.]

A-G74-176-2

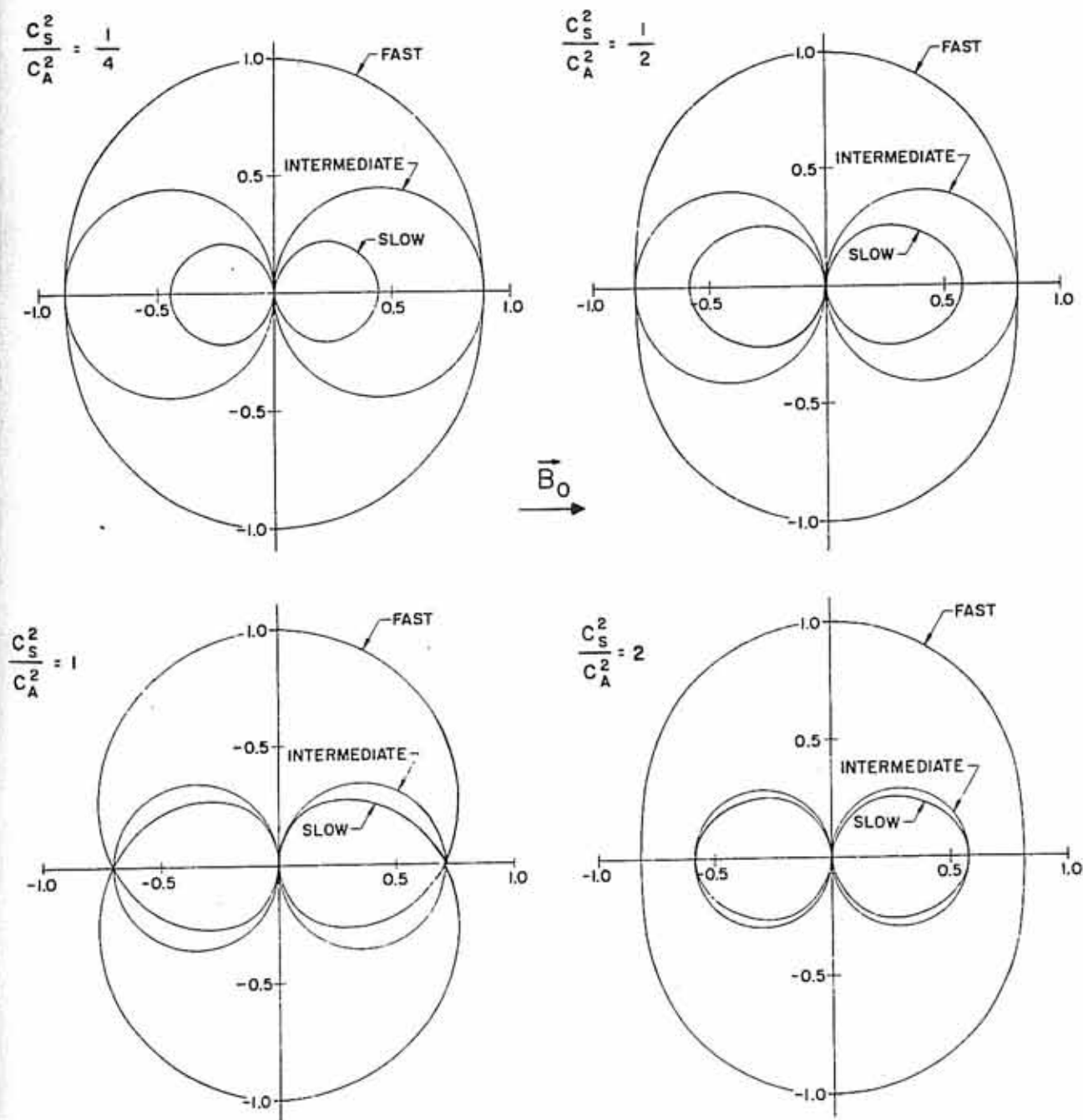


FIGURE 3

Figure 4 The three solutions to the two-fluid dispersion relation for a warm plasma, propagation direction with respect to the magnetic field $\theta = 45^\circ$, and $C_s^2/C_A^2 = 0.2$. The wave frequency ω is normalized to the ion gyrofrequency Ω_+ and the wave number k to C_s/Ω_+ . The dashed line labelled C_e estimates the electron thermal velocity for a hydrogen plasma with equal ion and electron temperatures. The lower left hand corner is the domain of validity for the MHD approximation. Below the ion gyrofrequency the three MHD waves propagate; between the electron and ion gyrofrequencies, the whistler and ion sound waves propagate; above the electron gyrofrequency the ion sound wave propagates. Coupling points occur near the electron and proton gyrofrequencies. The approximate expressions shown for the phase velocities are strictly valid only when $C_s^2/C_A^2 \ll 1$. [After Formisano and Kennel, 1969.]

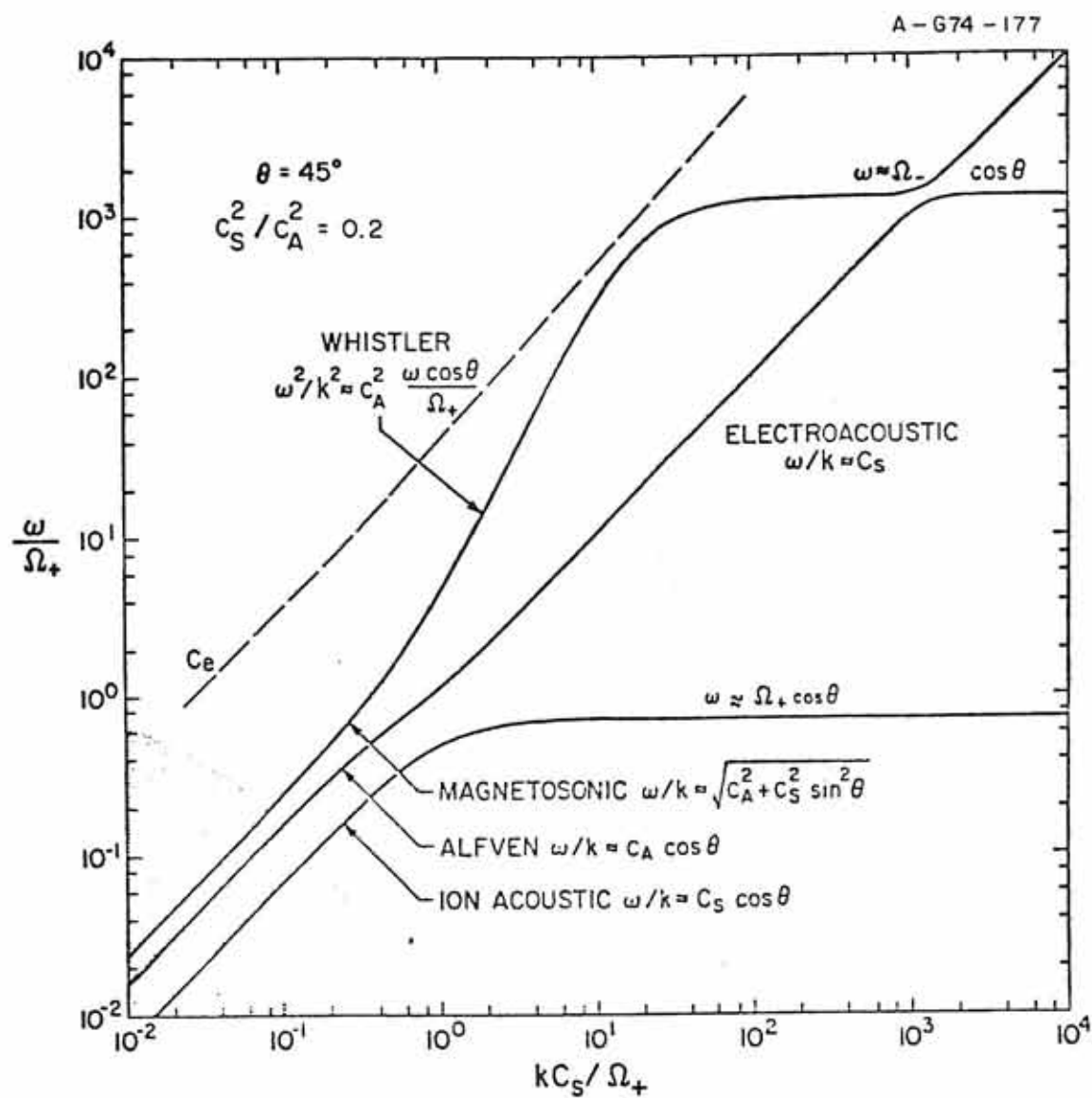


FIGURE 4

Figure 5 The properties of warm plasma propagation in ω/Ω_+ , c_s^2/c_A^2 parameter space. In each region is a polar plot whose radius is the plane wave phase velocity and whose angle is the angle of propagation relative to the magnetic field. The direction of the magnetic field is denoted by an arrow. The dotted reference circles have a radius c_s . The interaction diagonal indicates where the cold plasma parallel whistler phase velocity equals the sound speed. Parallel sound waves are slower than whistlers to the left and faster to the right of this line. [After Formisano and Kennel, 1969.]

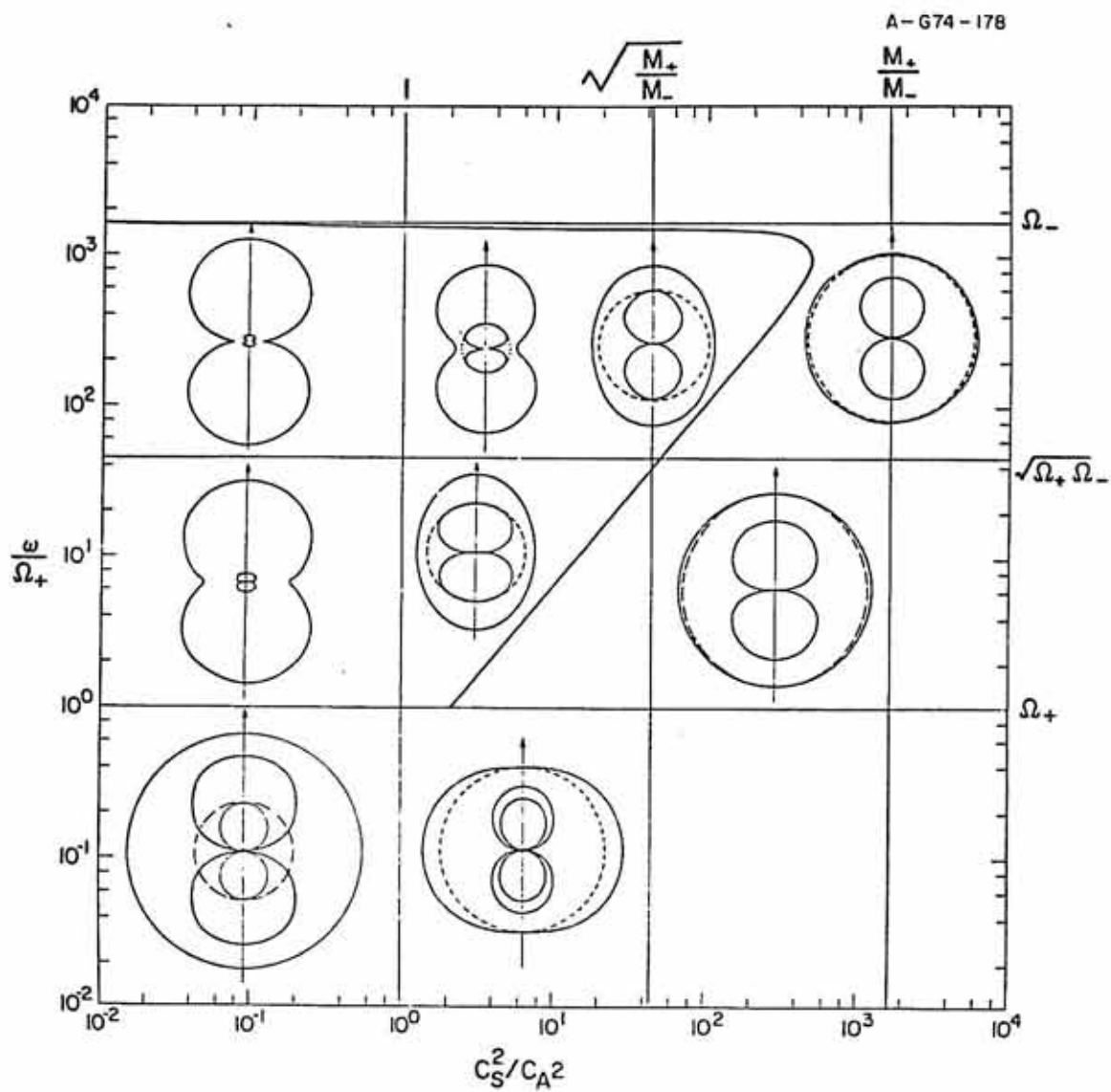


FIGURE 5

Figure 6 A schematic diagram of the perpendicular shock model with $\vec{B}(x) = B(x)\hat{z}$ and $\vec{E} = E\hat{x}$. The magnetic field gradient $\nabla B = |\partial B/\partial x|(-\hat{x})$ is related to the net electron drift current by $(4\pi/c)\vec{J} = \nabla \times \vec{B}$. The electric field is determined by charge separation. The guiding center trajectories in the x-y plane of ions (i) and electrons (e) indicate that only electrons undergo appreciable drift motion over the shock thickness scale length L_s .

C-G74-291

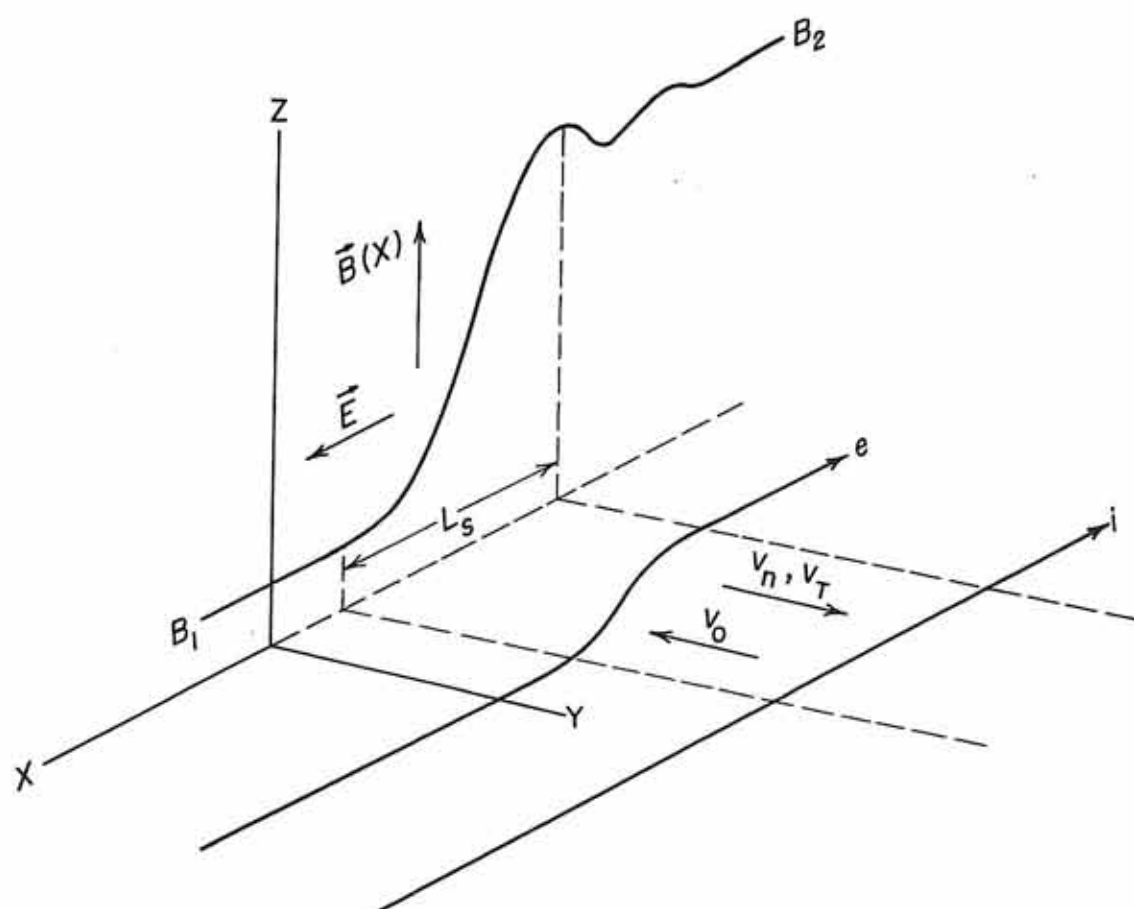


FIGURE 6

Figure 7 A typical bow shock crossing as detected by the IMP-6 plasma wave experiment. Average measurements (5.12 second time constant) are plotted as vertical lines; peak measurements (0.1 second time constant) are plotted as dots. The shock transition occurs at about 1048 UT. The electric field measurements (left) show upstream plasma oscillations at 31.1 kHz after 1048 UT. Shock parameters, $M_A = 7.7$, $\beta = 0.89$, $T_e/T_i = 3.3$, $\psi(\vec{B}, \hat{n}) = 73^\circ$.

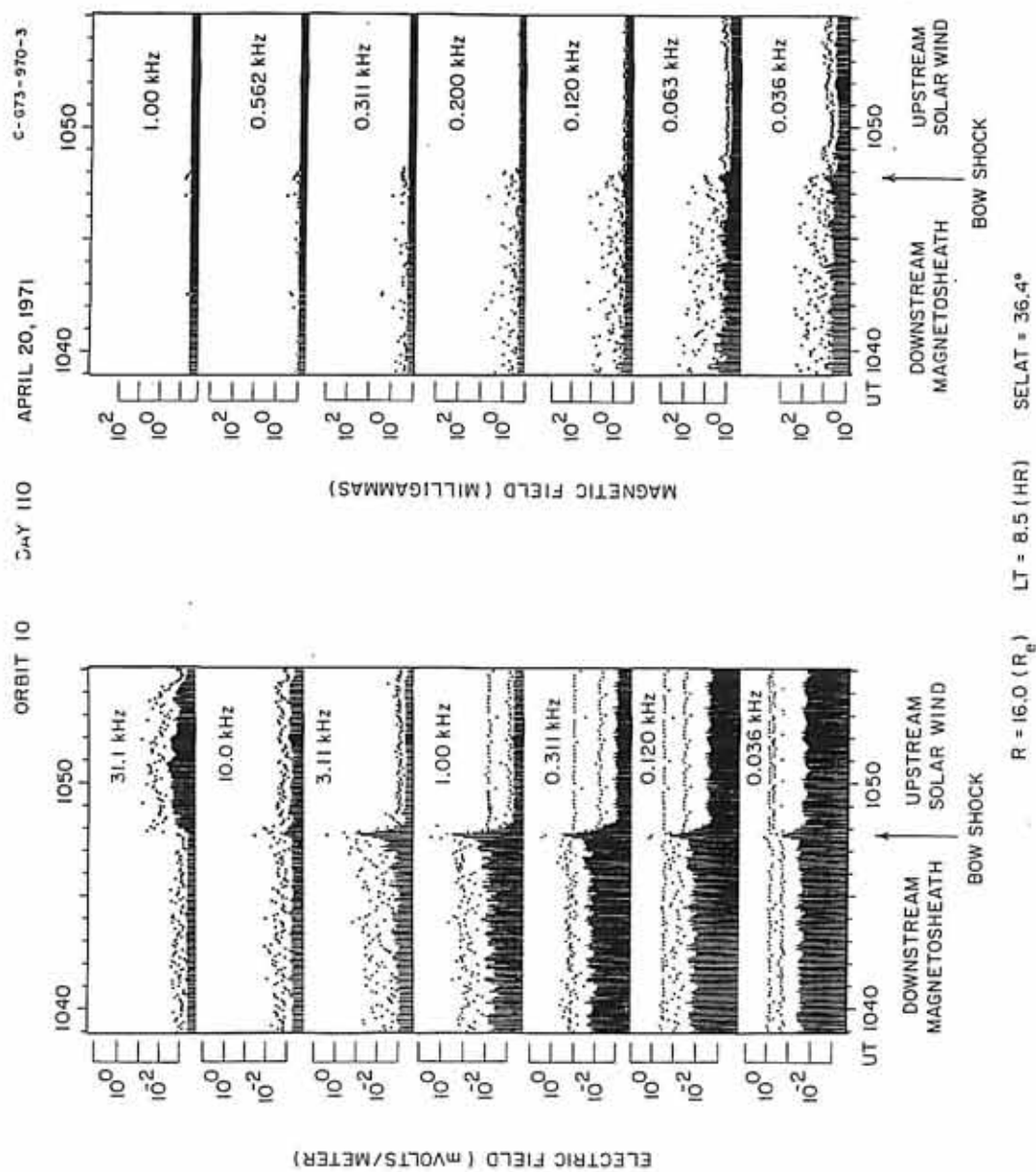


FIGURE 7

Figure 8 A double crossing of the earth's bow shock as detected by the IMP-6 plasma wave experiment. The bow shock was very nearly a perpendicular shock during these crossings. Shock parameters, $M_A = 6.0$, $\beta = 0.54$, $T_e/T_i = 3.3$, $\psi(\vec{B}, \hat{n}) = 92^\circ$.

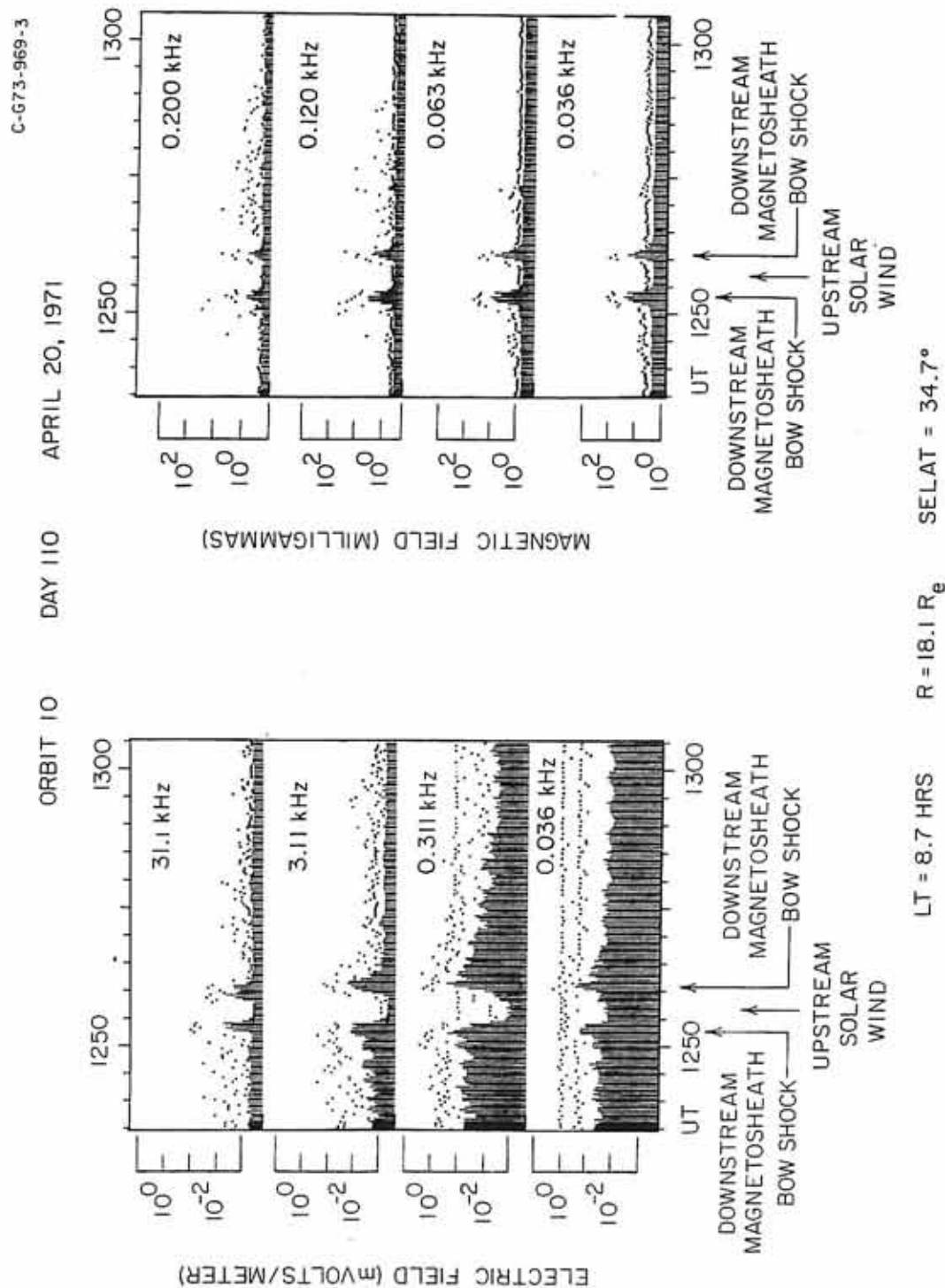


FIGURE 8

Figure 9 The electric field spectra, based on average measurements, for the crossing at 1252 UT in Figure 8. The time indicated is for the first spectrum with the averaging time, 5.12 seconds between succeeding spectra thereafter. Snapshot 7 is the shock electric field spectrum.

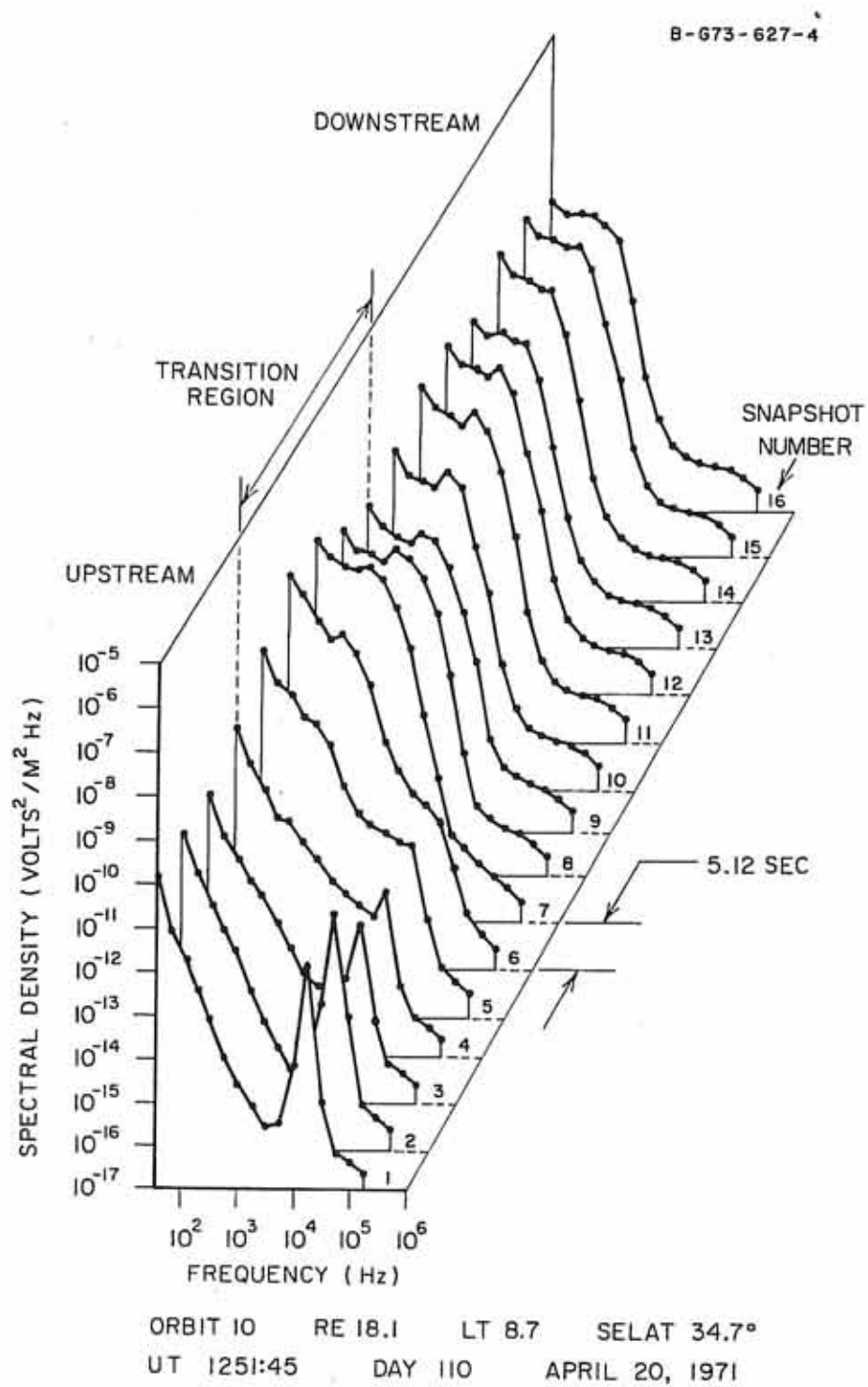


FIGURE 9

Figure 10 The magnetic field spectra, based on average measurements, for the crossing at 1252 UT in Figure 8 and corresponding to the electric field spectra in Figure 9. Snapshot 6 is the shock magnetic field spectrum.

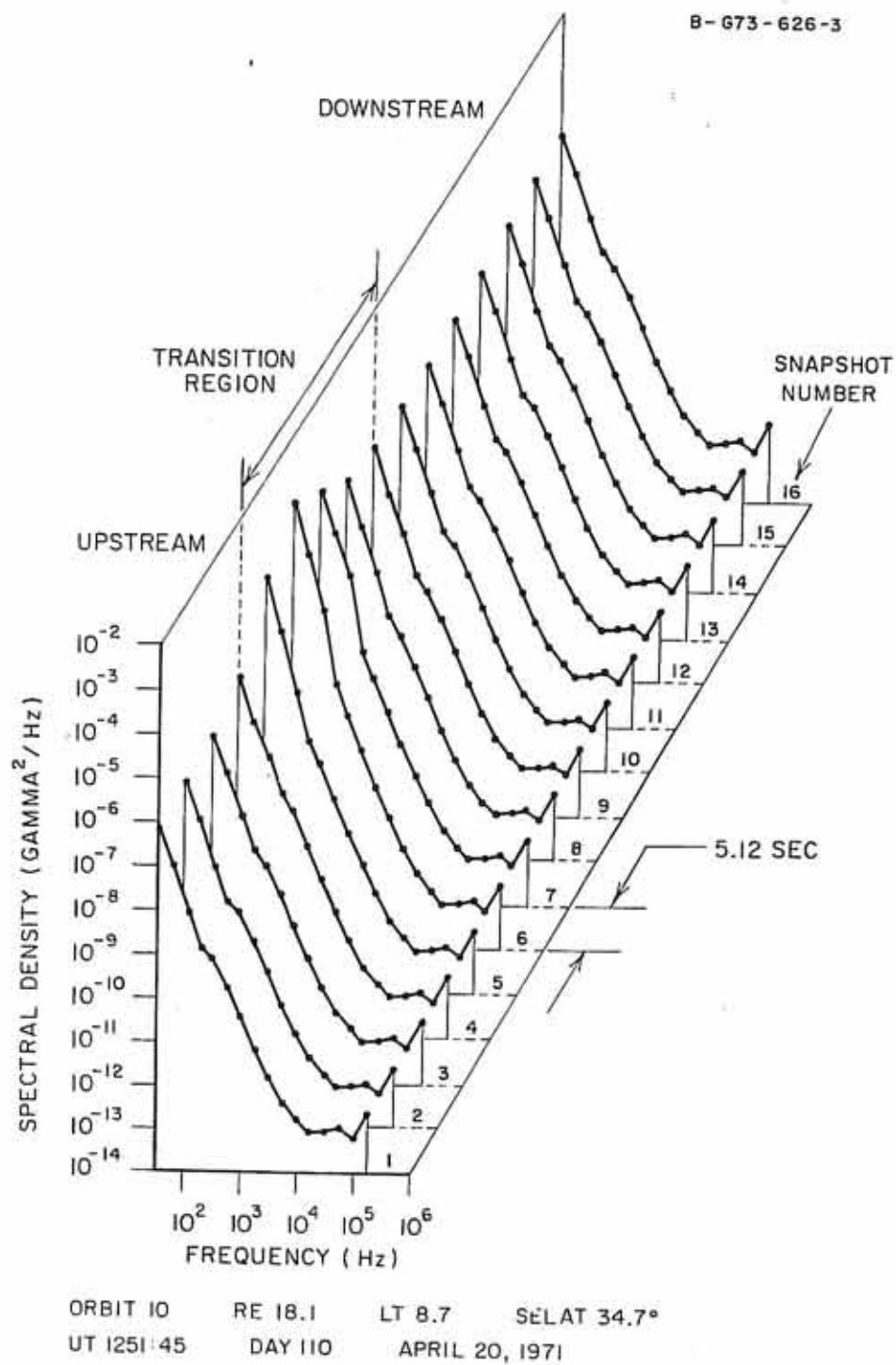


FIGURE 10

Figure 11 The shock electric field spectrum $E^2(\omega)_{sh}$ selected on the basis of the r. m. s. electric field amplitude. The peak spectrum obtained during the averaging time of the average measurements is also shown. The two distinct components in the shock electric field spectrum are shown by dashed lines.

A-673-690-5

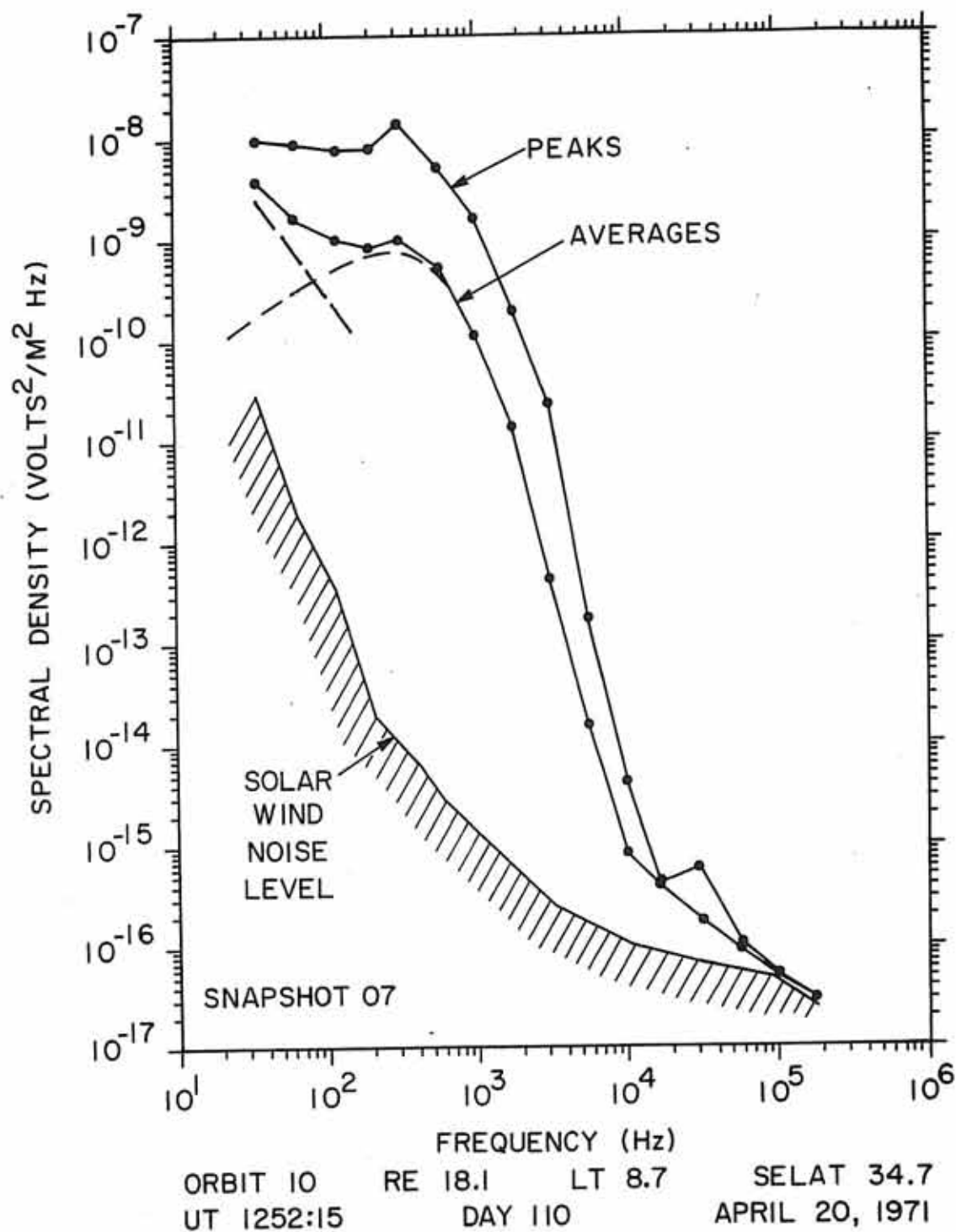


FIGURE II

Figure 12 The shock magnetic field spectrum $B^2(\omega)_{sh}$ for the shock crossing of 1252 UT. The characteristic frequency dependence f^{-4} is present in both peak and average spectra. The electron gyrofrequency $f_{ge} \sim 350$ Hz.

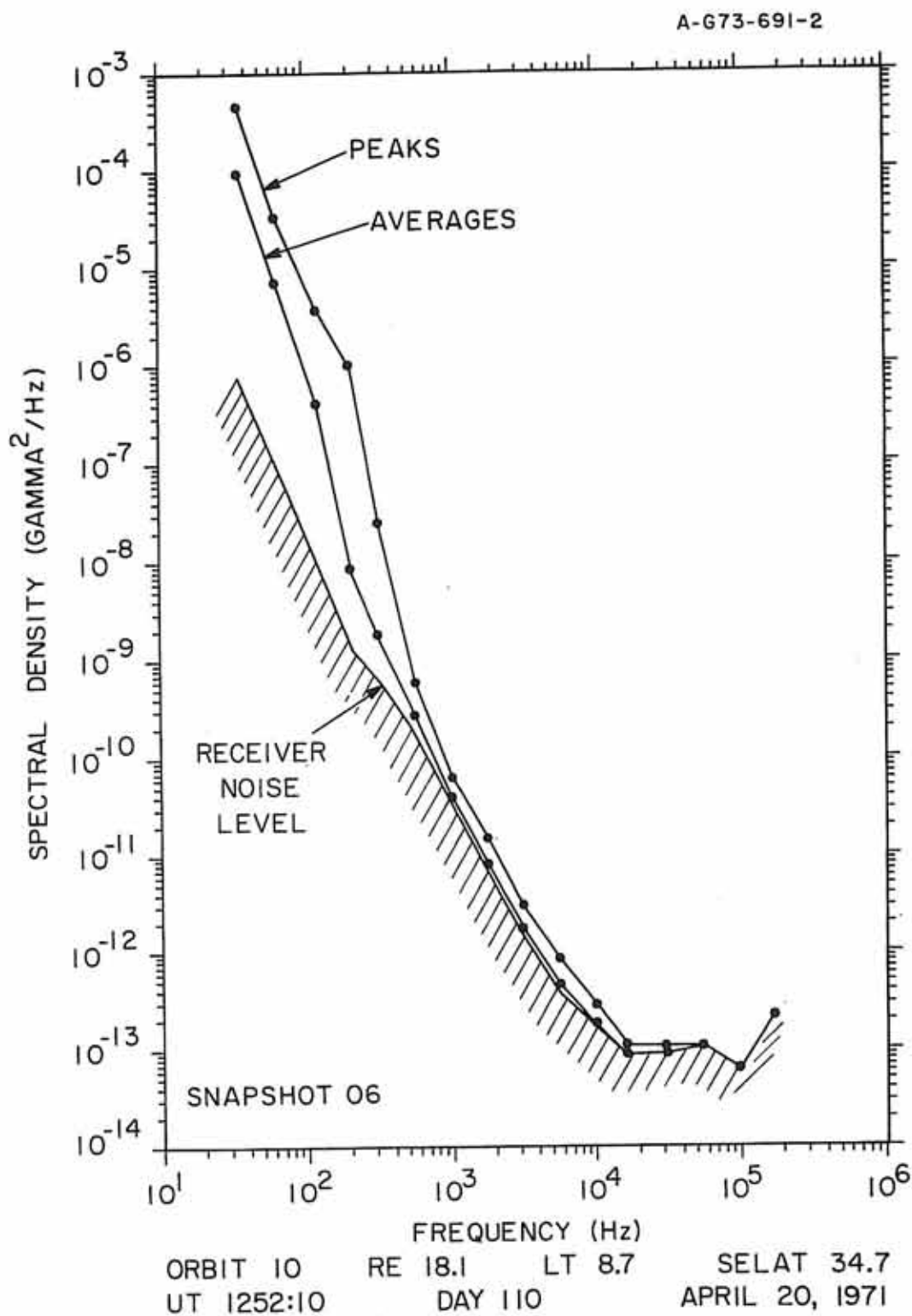


FIGURE 12

Figure 13 A representative distribution of electric field shock spectra, average and peak measurements. The average spectra show that the broad peak in the electric field spectra becomes more distinct as the overall intensity of the spectra increases up to some intermediate range, and then becomes less distinct as the very low frequency electric field spectra density saturates. The peak spectra are generally similar to the average spectra in shape, but range up to an order of magnitude more intense.

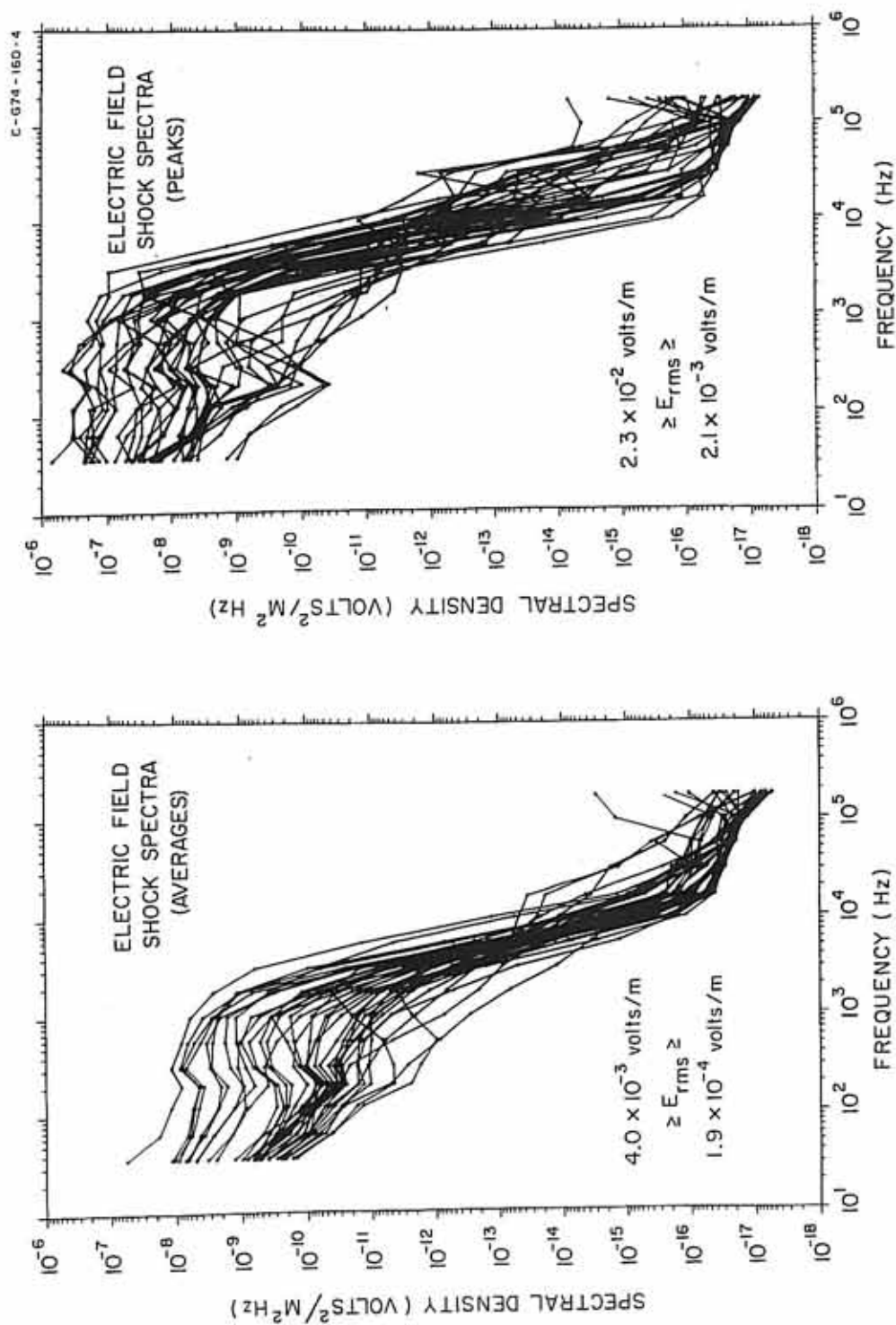


FIGURE 13

Figure 14 Representative distribution of magnetic field shock spectra, average and peak measurements, corresponding to the electric field spectra of Figure 13. Some of the peak spectra indicate the presence of distinct wave modes.

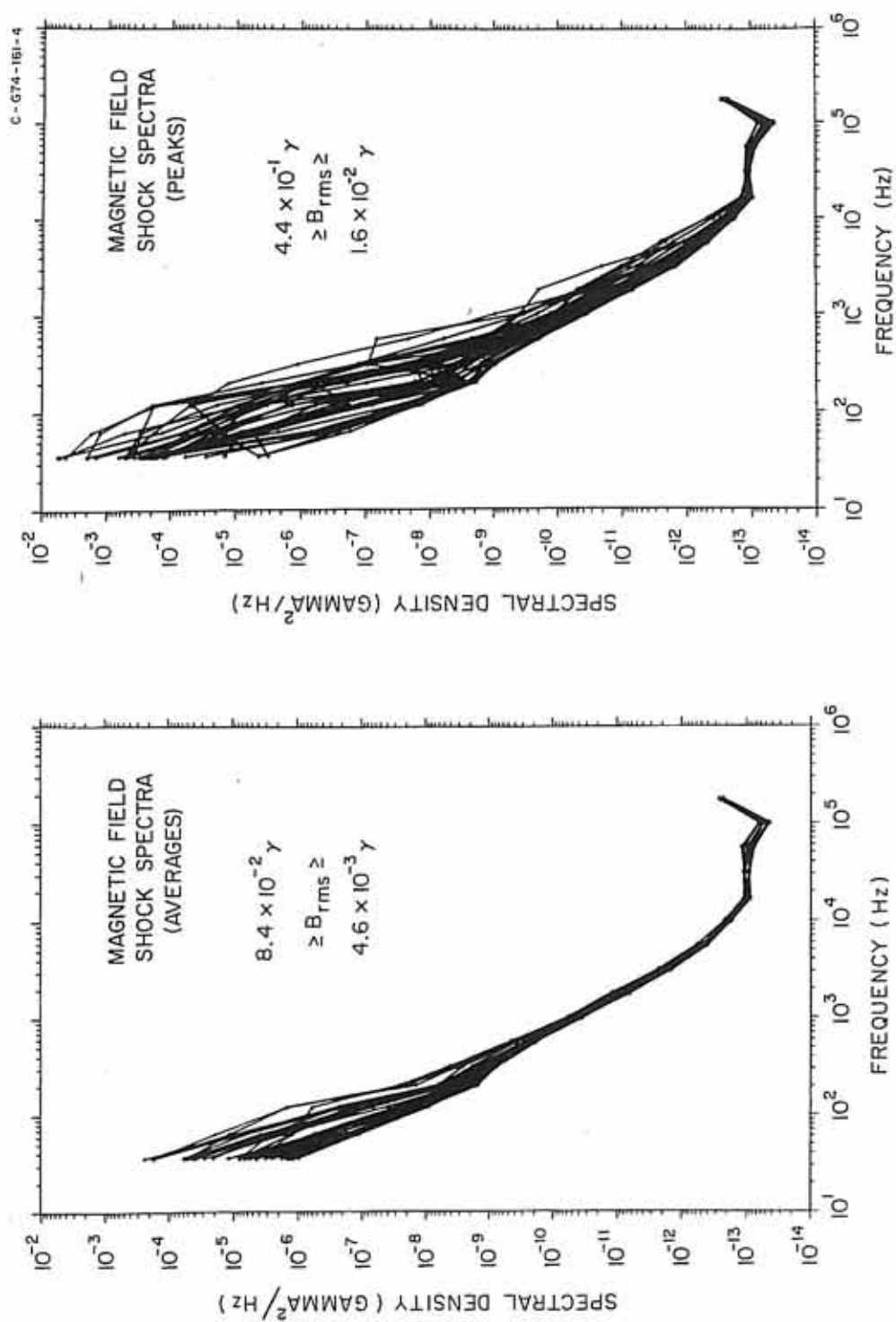


FIGURE 14

Figure 15 The ratio of electric energy density to magnetic energy density for the shock crossing of 1252 UT, Figure 8. The low frequency portion of snapshots 5, 6, and 7 is consistent with whistler waves. At higher frequencies electrostatic noise is the dominant wave mode. The region of electrostatic noise is observed to broaden toward lower frequencies further into the transition region.

B-G73-932-3

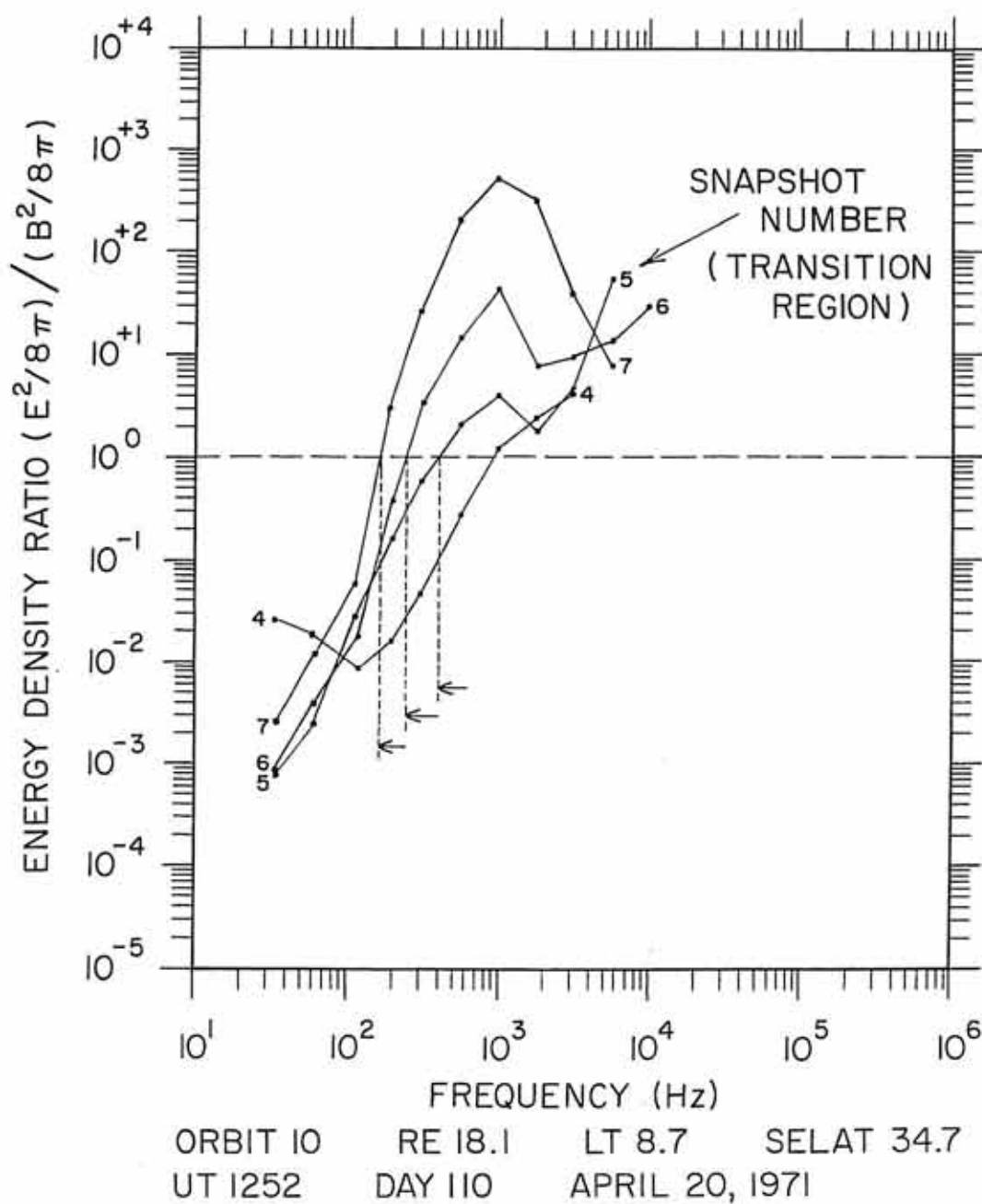


FIGURE 15

Figure 16 A representative distribution of energy density ratios for 10 shock crossings, selected at random from the shock electric and magnetic field spectra.

B-674-256-1

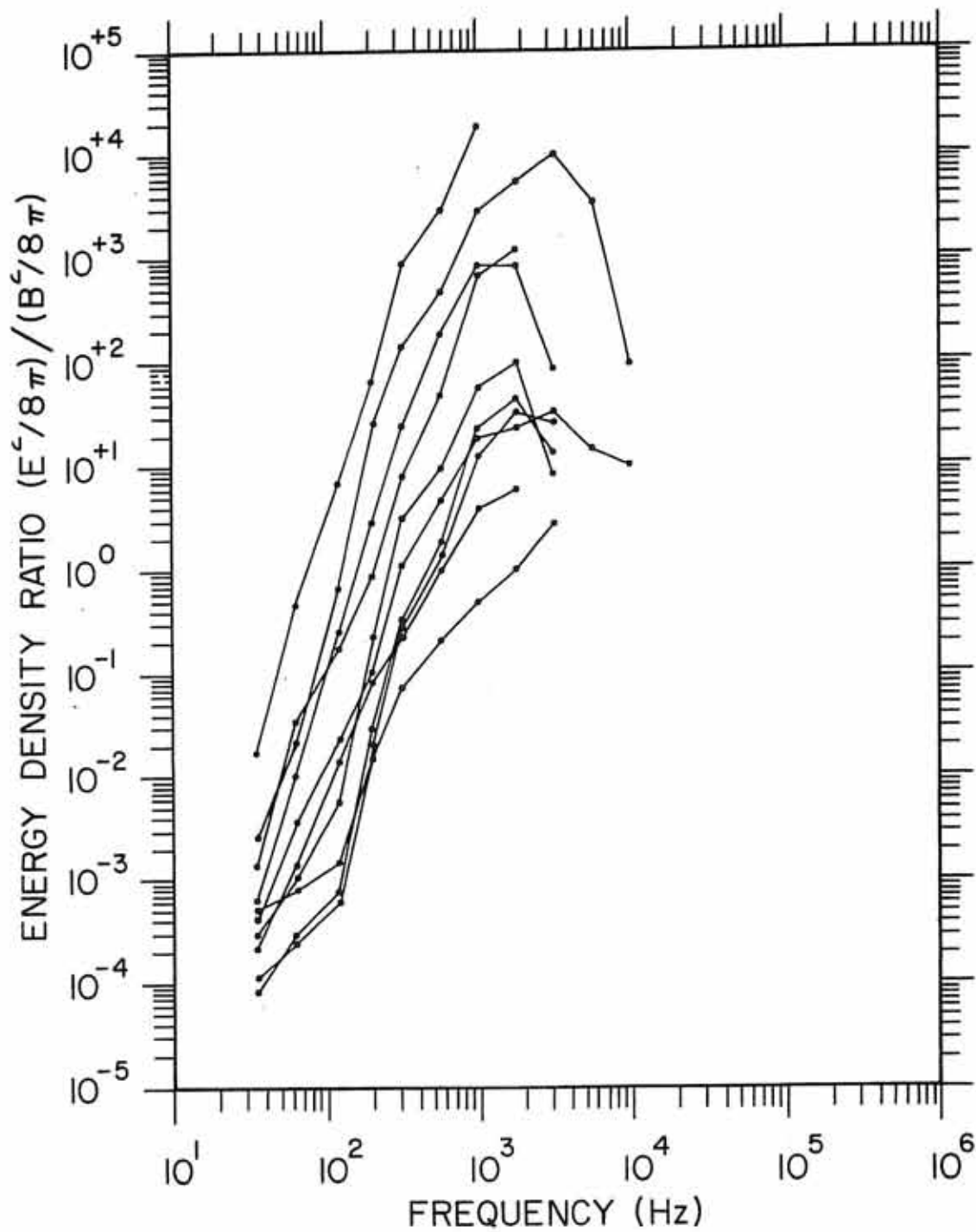


FIGURE 16

Figure 17 Wideband spectra for the shock crossings of Figure 8, for frequencies 0 - 500 Hz. The turbulence of the shock transition appears more homogeneous than downstream turbulence for both electric and magnetic fields. Discrete noise structure characterizes the downstream regions.

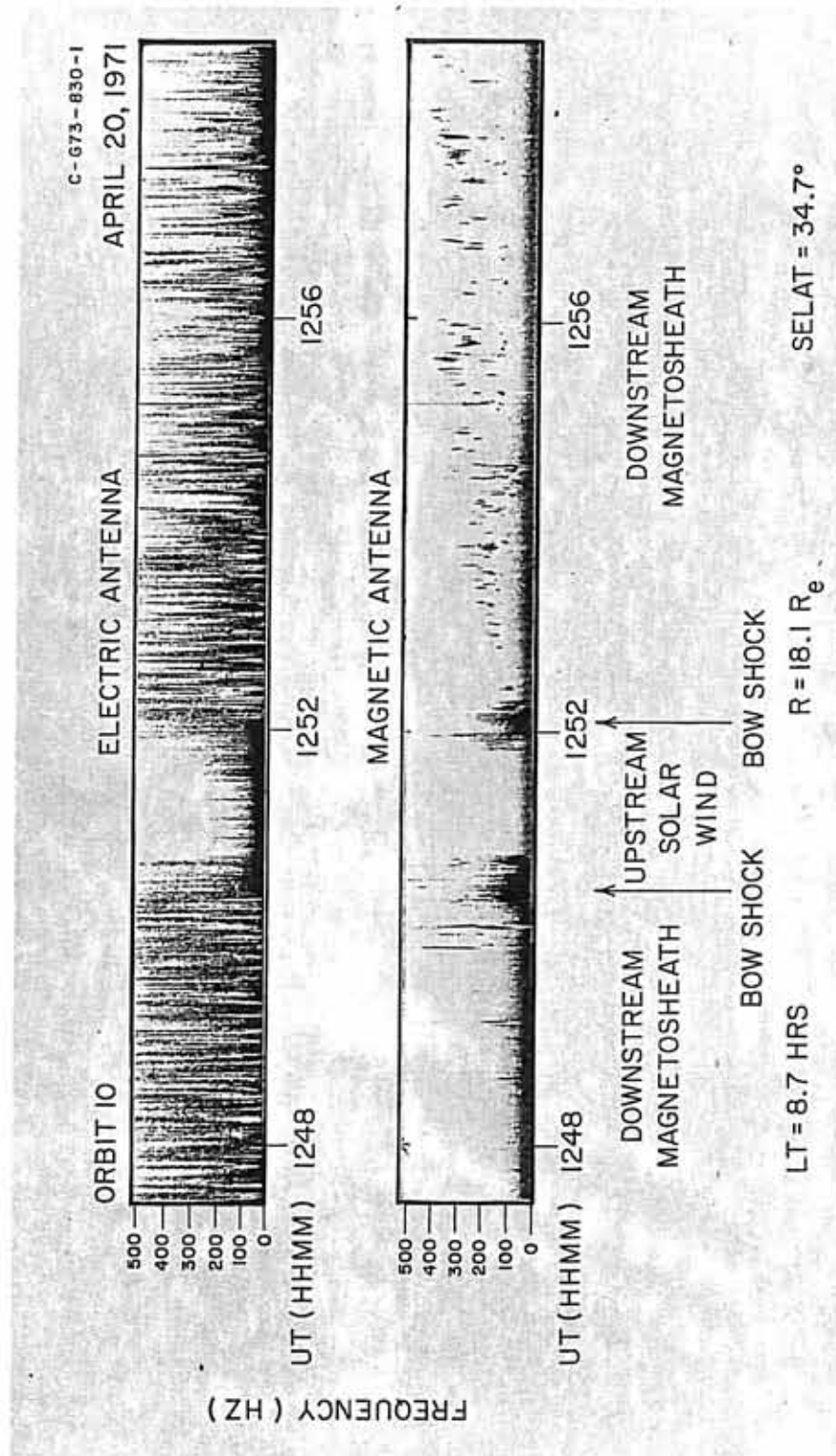


FIGURE 17

Figure 18 Expanded time scale wideband spectra for the second shock crossing of Figures 8 and 17. The shock turbulence retains a homogeneous appearance, while the downstream noise shows a few 'parabola shaped' bursts in the electric field.

C-673-306-2

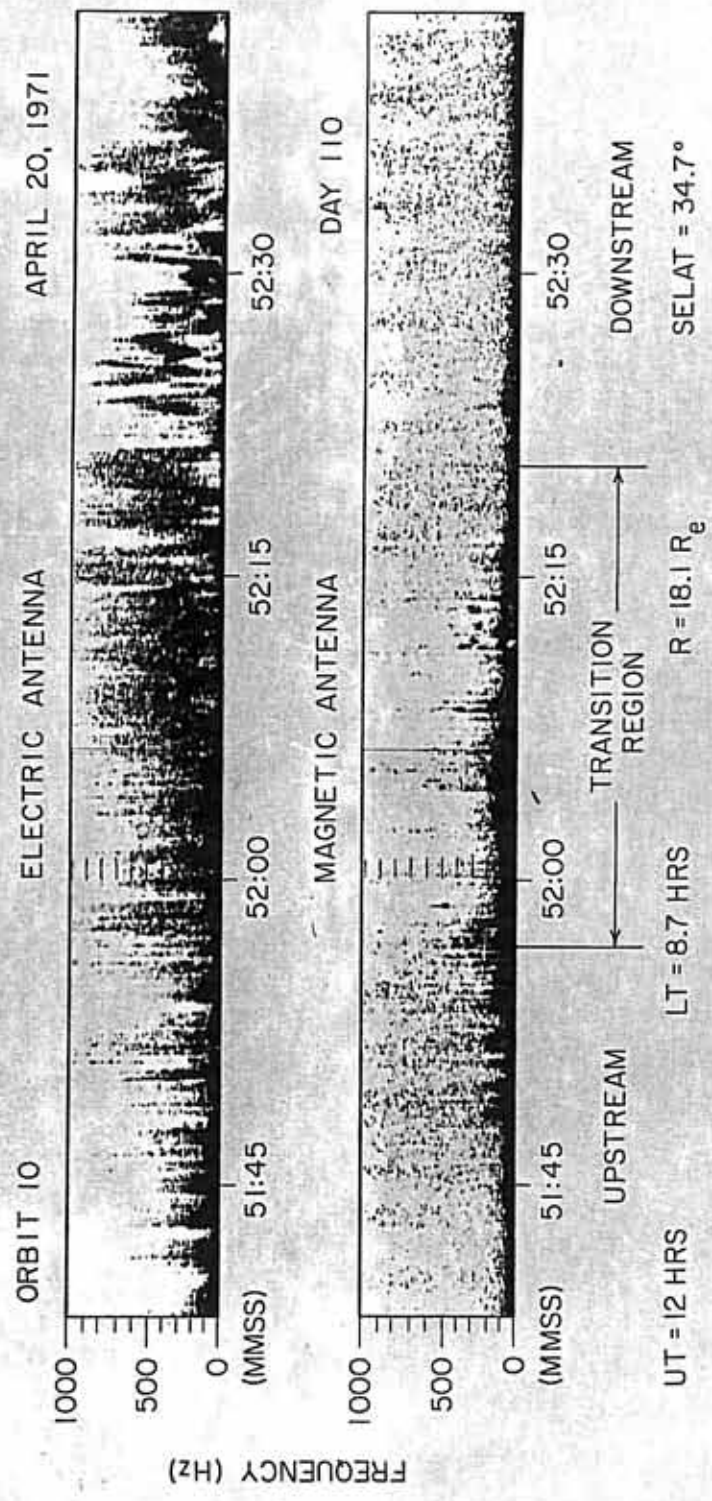


FIGURE 18

Figure 19 Upstream electron plasma oscillations and 'precursor' encountered a few minutes before the shock crossing at about 1548:30 UT. The rapid-sample measurements A and B give the spin modulated electric field amplitudes shown in the two polar plots. The electric field vector of these waves is predominantly aligned parallel to the static magnetic field. Shock parameters, $M_A = 4.8$, $\beta = 0.34$, $T_e/T_i = 3.3$, $\psi(\vec{B}, \vec{n}) = 111^\circ$.

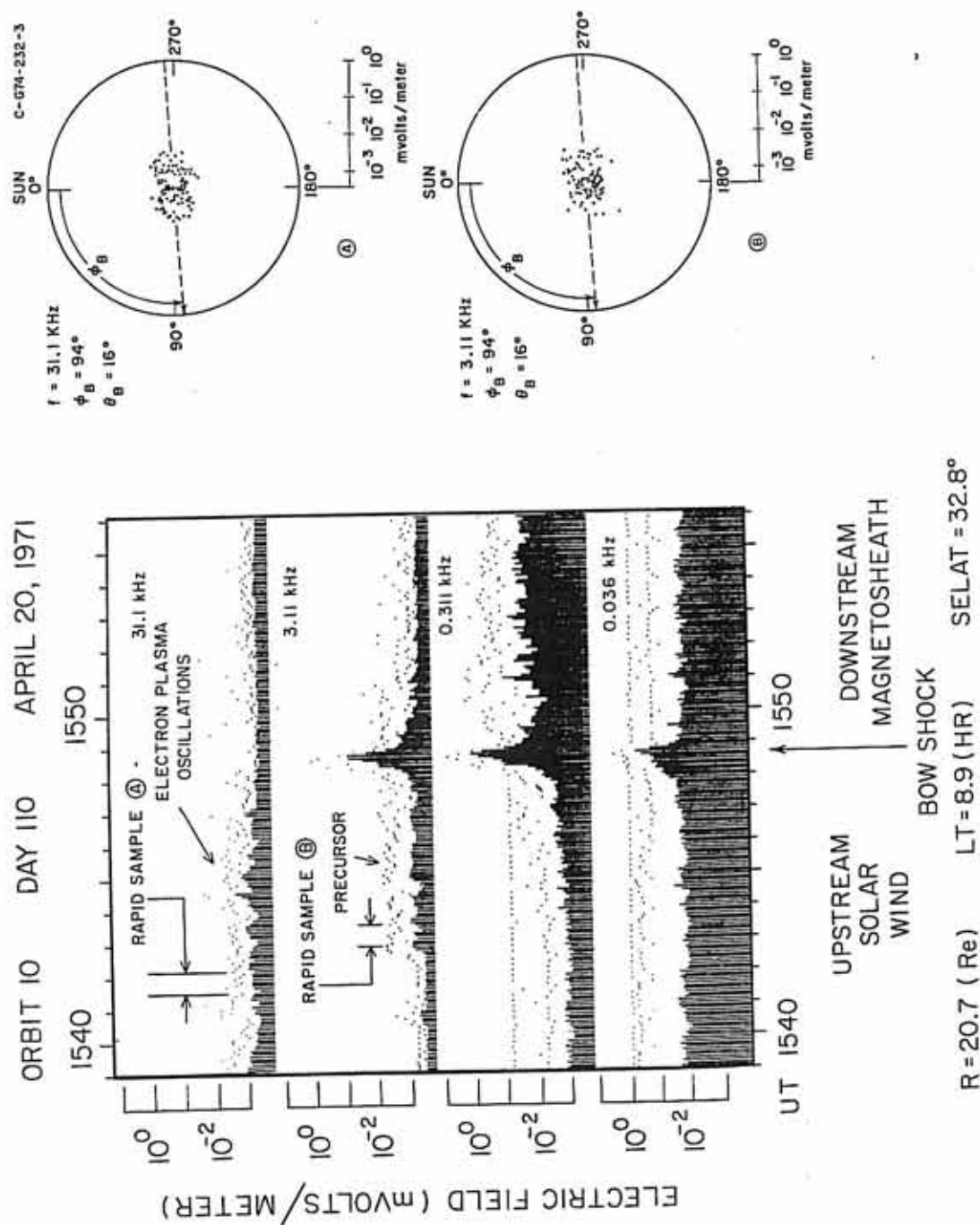


FIGURE 19

Figure 20 Rapid-sample measurement of electric field at 3.11 kHz for the bow shock transition and downstream regions. The electric field fluctuations are correlated with magnetic field gradients in both the transition and downstream regions. The polar plot in the upper right corner shows the spin modulation of electric field amplitude for the transition region, interval a to b. The downstream electric field fluctuations, indicated by the envelope of exponential decay, do not show spin modulation effects (middle and lower right polar plots). Shock parameters, $M_A = 4.8$, $\beta = 0.28$, $T_e/T_i = 6.7$, $\psi(\vec{B}, \hat{n}) = 87^\circ$.

D-674-289

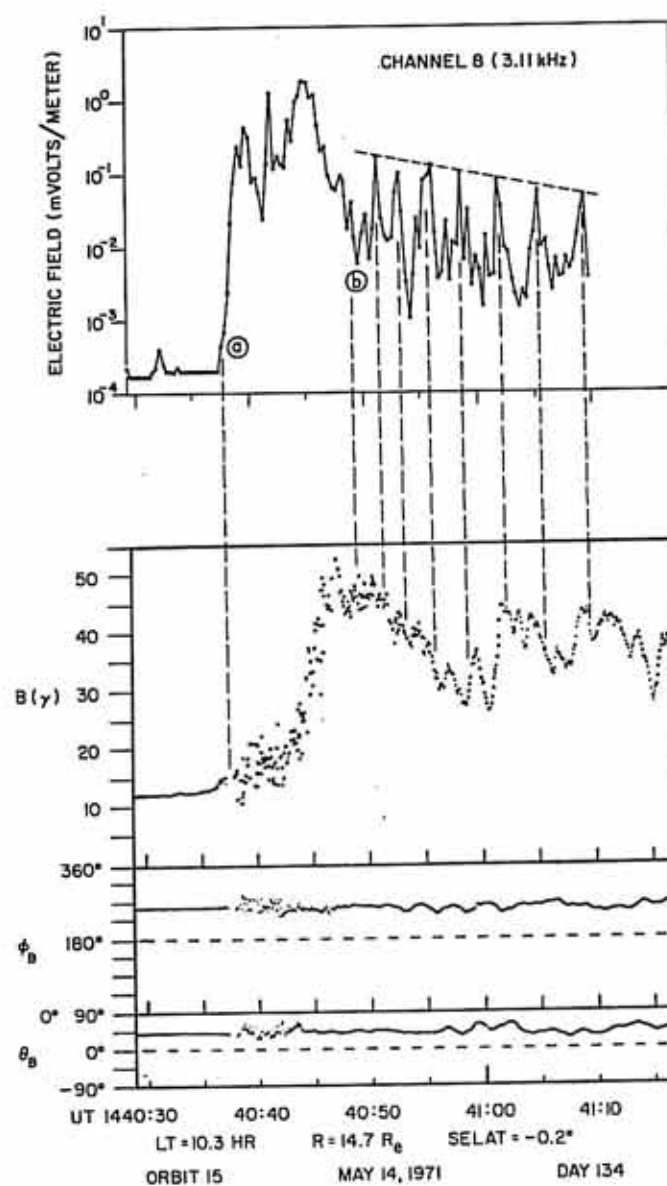


FIGURE 20

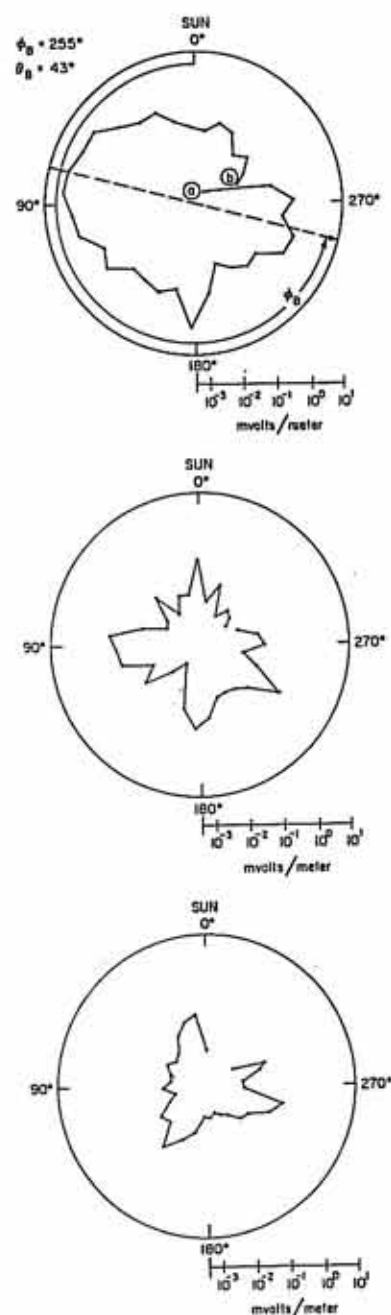
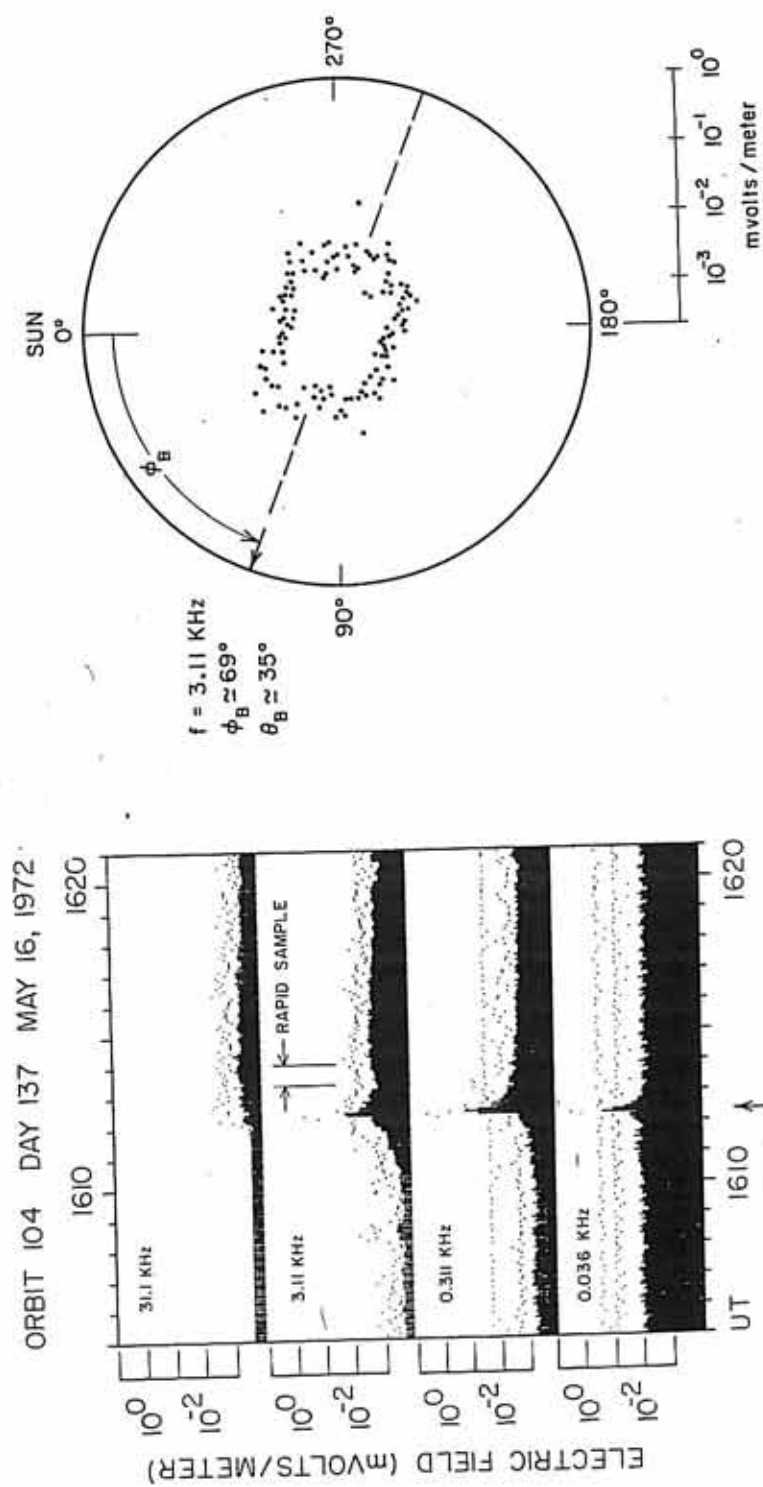


Figure 21 A series of rapid-sample measurements of the magnetosheath electric field turbulence which shows that the electric field vector of this noise is aligned parallel to the static magnetic field. Shock parameters, $M_A = 1.8$, $\beta = 0.03$, $T_e/T_i = 4.0$, $\psi(\hat{B}, \hat{n}) = 95^\circ$.

C-674-219-2



$R = 29.7 \text{ (Re)}$ $LT = 9.4 \text{ (HR)}$ $SELAT = 2.0^\circ$

FIGURE 21

Figure 22 The plot of $E_{rms,2}$ against T_e/T_i which shows a strong positive correlation. The dashed diagonal line is the line of regression for a least squares fit to the equation $\log y = ax + b$, where $y = E_{rms,2}$ and $x = T_e/T_i$. The degree of dispersion of the slope of the regression line, which is the important measure of association, is indicated by the small error bars at $\pm 2.576 \sigma(\bar{y})$. Correlations with parameters not included in this fit contribute to the large error bars at $\pm \sigma(y)$. The solid diagonal line indicates an apparent lower threshold for electrostatic turbulence.

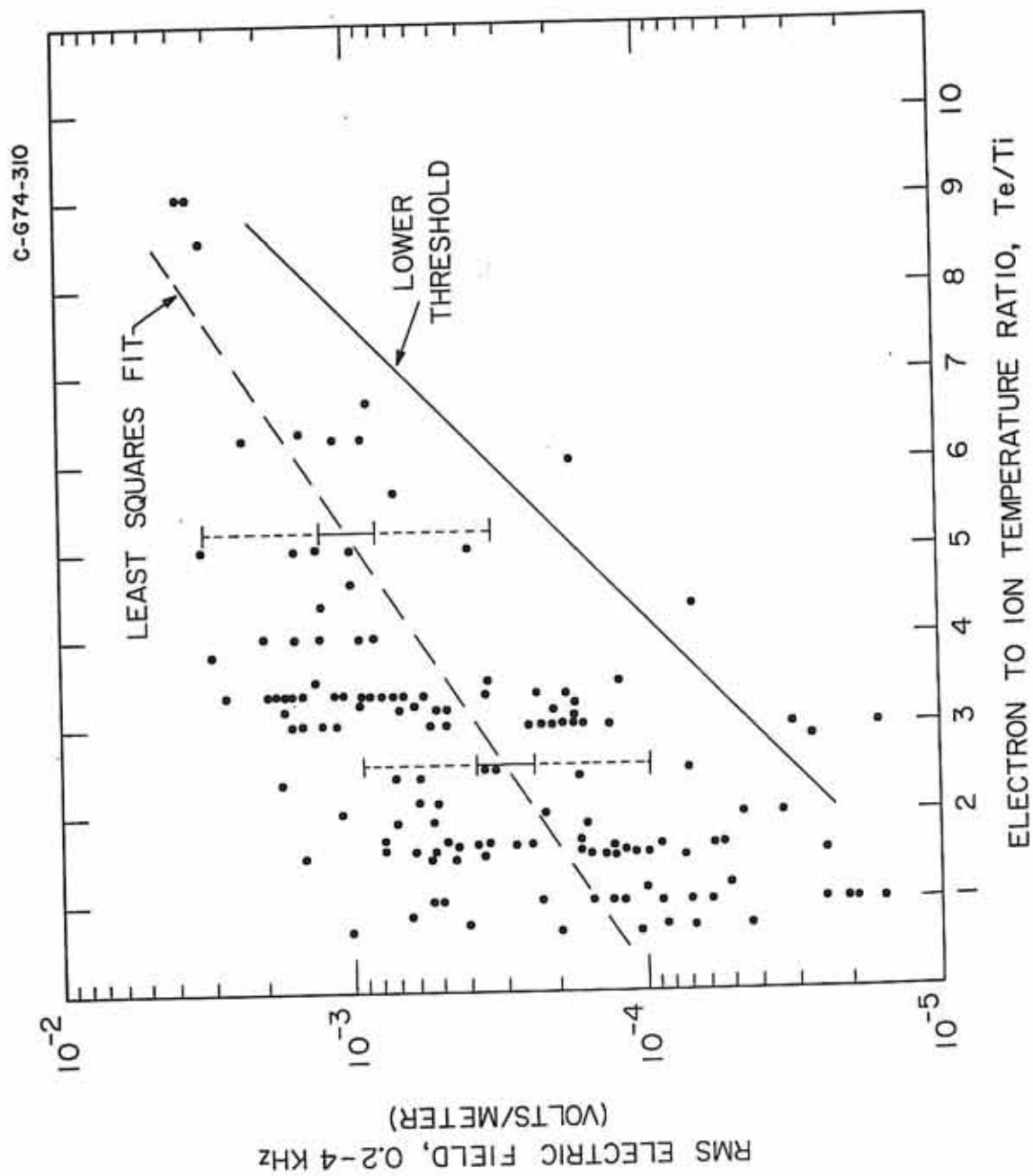


FIGURE 22

Figure 23 The plot of $E_{\text{rms},2}$ against C_s (proportional to $(T_e + T_i)^{1/2}$) showing a strong negative correlation for a least squares fit to $\log y = ax + b$ where $y = E_{\text{rms},2}$ and $x = C_s$. The error bars have the same meaning as in Figure 22.

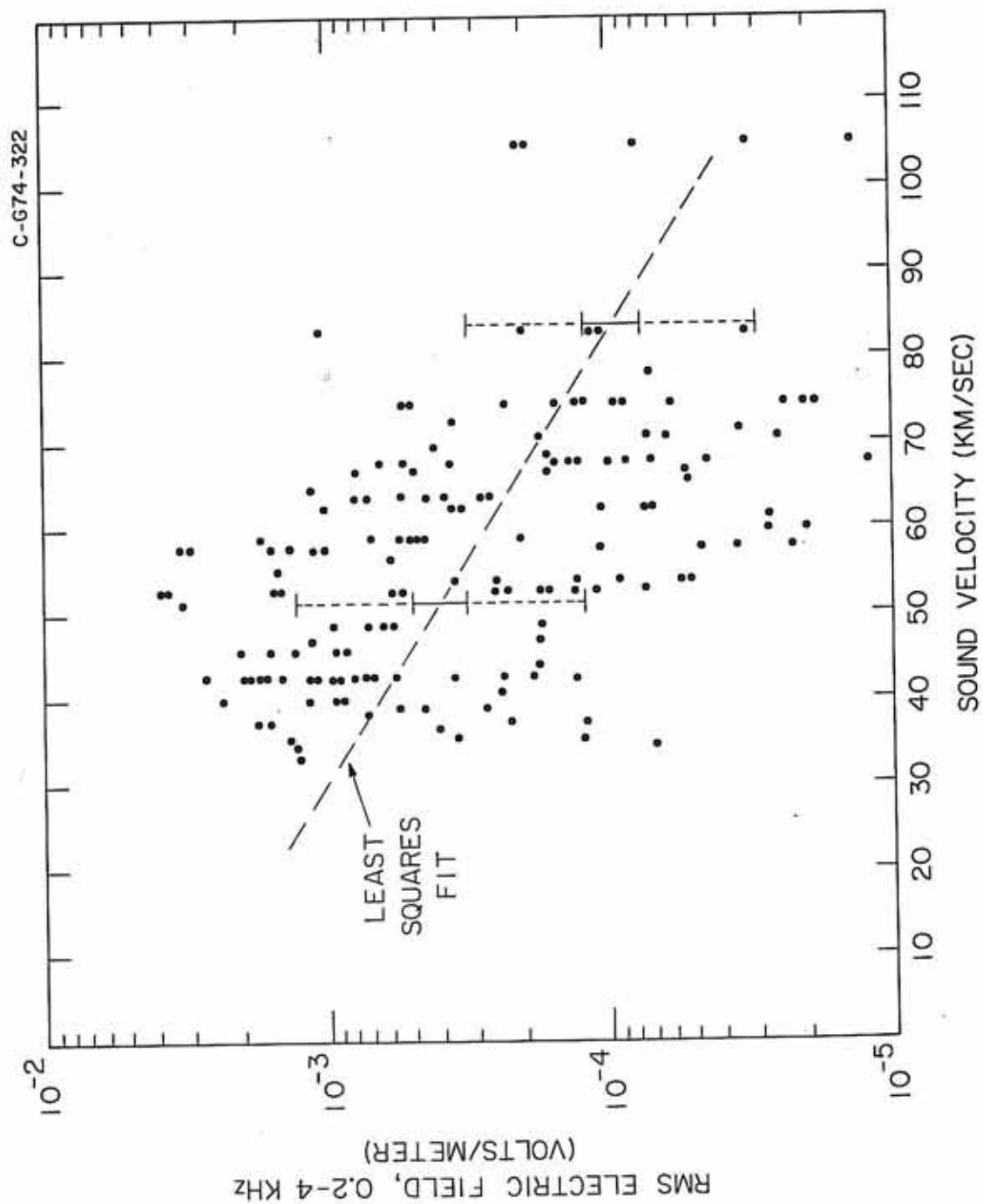


FIGURE 23

Figure 24 The plot of $E_{\text{rms},1}$ against C_s (proportional to $(T_e + T_i)^{1/2}$) showing a negative correlation almost as strong as for $E_{\text{rms},2}$ and C_s . The error bars have the same meaning as in Figure 22.

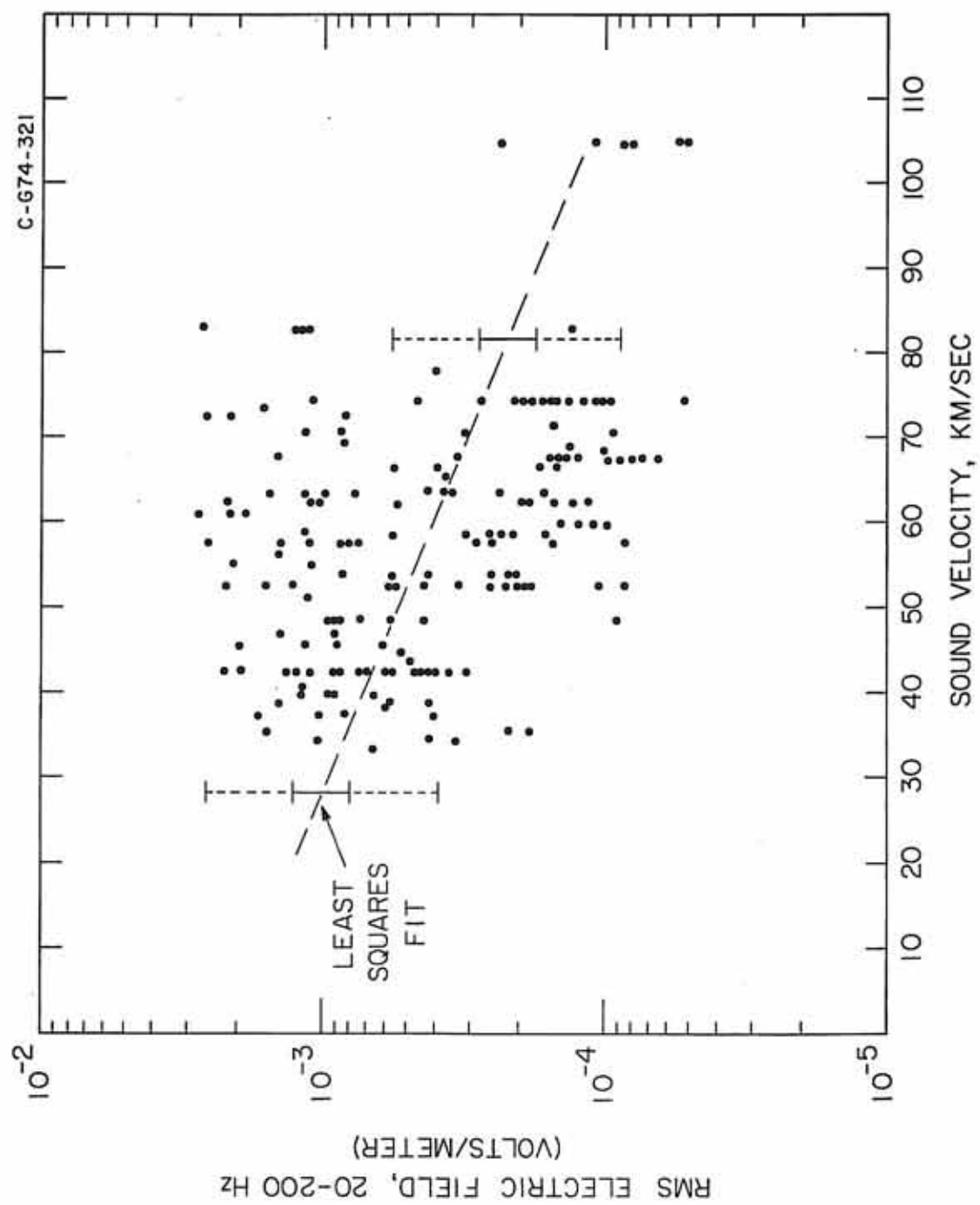


FIGURE 24

Figure 25 The plot of B_{rms} against $\psi(\vec{B}, \vec{V}_{SW})$, the angle between the upstream vectors of magnetic field and solar wind velocity. $\psi(\vec{B}, \vec{V}_{SW})$ is the only angle with which shock turbulence had a significant correlation. The error bars have the same meaning as in Figure 22.

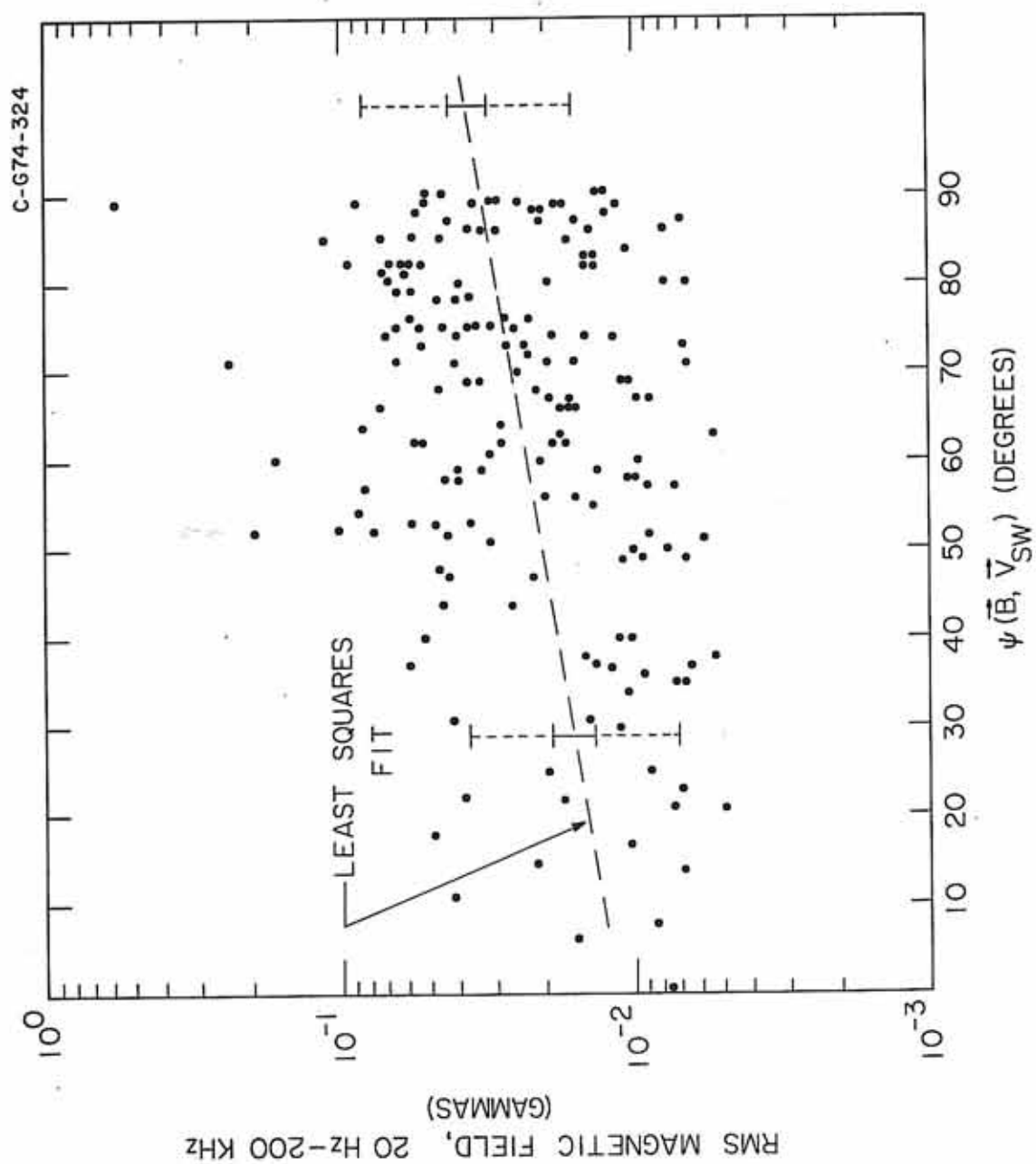


FIGURE 25